ORNL POSITIVE ION NEUTRAL BEAM PROGRAM*

J. H. Whealton, H. H. Haselton,† G. C. Barber, C. W. Blue,
W. K. Dagenhart, R. C. Davis, W. L. Gardner, J. Kim, M. M. Menon,
N. S. Ponte, P. M. Ryan, D. E. Schechter, S. W. Schwenterly,
W. L. Stirling, C. C. Tsai, and R. E. Wright

CONF-780662--1

NOTICE
This report was prepared as an account of work sponsored by the United States Government. Neither the United States nor the United States Department of Energy, nor any of their employees, nor any of their contractors, subcontractors, or their employees, makes any warranty, express or implied, or assumes any legal liability or responsibility for the accuracy, completeness or usefulness of any information, apparatus, product or process disclosed, or represents that its use would not infringe privately owned rights.

The neutral beam group at Oak Ridge National Laboratory has constructed neutral beam generators for the ORMAK and PLT devices, is presently constructing neutral beam devices for the ISX and PDX devices, and is contemplating the construction of neutral beam systems for the advanced TNS device. These neutral beam devices stem from the pioneering work on ion sources of G. G. Kelley and O. B. Morgan.[1-3] We describe the ion sources under development at this laboratory, the beam optics exhibited by these sources, as well as some theoretical considerations, and finally the remainder of the beamline design.

I. ION SOURCES

The ion sources considered at this laboratory are (a) the hollow cathode cusp field duoPIGatron, (b) magnetic multipole cusp field source, and (c) the $LaBr_6$ hollow cathode cusp field source. The principal line of sources under development originates from modifications of a duoplasmatron and is called a duoPIGatron.[4-8] It consists, as shown schematically in Fig. 1, of a thermionic cathode discharge followed by a collision dominated discharge followed by axial extraction. More detailed illustrations of duoPIGatron ion sources and cusp magnetics are found in Refs. 4-9. The plasma generator consists of hot cathodes, an intermediate electrode, anode 1, anode 2, magnetic cusp fields, and a plasma grid. The intermediate electrode serves as a magnetic pole to provide an axial magnetic field, the source field, in the anode region. A pulsed arc voltage is applied between the anodes and hot cathodes. The intermediate electrode and target cathode are returned to the arc supply positive terminal through appropriate biasing resistors.

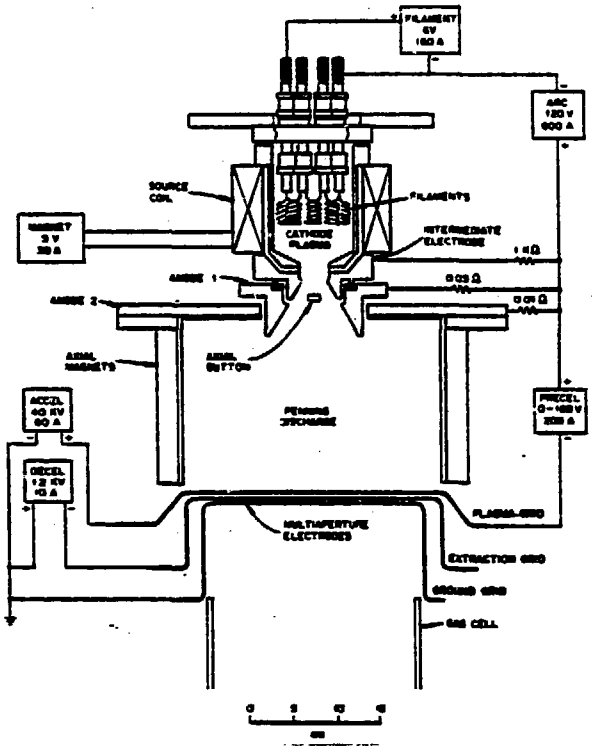

Fig. 1. Schematic of 22-cm ion source.

The source contains a cathode plasma and a PIG plasma separated by an intermediate plasma double layer. The cathode plasma is produced within the intermediate electrode chamber by primary electrons emitted from the hot cathodes. In this region of zero magnetic field, the plasma density is determined essentially by the arc current and the gas pressure, which operates at a relatively low electron kinetic energy of <30 eV.

The anode plasma is produced in the region enclosed by the anodes, the intermediate electrode, and plasma grid. This anomalous glow discharge is created essentially by energetic electrons which originate from the cathode plasma and which are accelerated through the double layer separating the cathode and anode plasma. The electrons are then confined by the applied magnetic field and ionize the gas in the upper region of anode 1 and anode 2 (Fig. 1) as they oscillate between the intermediate electrode and the plasma electrode. Because of their high energy, they create a dense anode plasma; consequently, the density of the anode plasma is mainly affected by the applied magnetic field, gas pressure, arc voltage, and arc current.

While the cathode plasma works as an electron source and supplies ionizing electrons to the anode discharge, the anode plasma works as a source of ions and supplies ions to the extraction electrodes in order to form a high current ion beam. The double layer works as a controlling mechanism which determines the anode plasma uniformity and the source reliability. The axial potential as inferred from the discharge mechanism and deduced from measurements with a Langmuir probe is shown in Fig. 2.

The applied magnetic field in the anode region consists of the axial field of the source electromagnet and the azimuthal cusp field of the permanent magnets. The axial field, originating from the intermediate electrode channel, controls the radial distribution of ionizing electrons in the anode region and thus influences the uniformity of the plasma created. Figure 3, the density profile as measured by a Langmuir probe in a plane 1 cm above the plasma grid, indicates that as the magnetic field is lowered, the plasma uniformity is improved but the density is lowered. With the permanent magnet on anode 2 to form the cusp field, the confinement of the ionizing electrons and the plasma creat

MASTER

*Research sponsored by the Office of Fusion Energy (ETM), U.S. Department of Energy under contract W-7405-eng-26 with the Union Carbide Corporation.

†Head of ORNL neutral beam program.

NOTICE
PORTIONS OF THIS REPORT ARE ILLEGIBLE. It has been reproduced from the best available copy to permit the broadest possible availability.

MN ONLY

By acceptance of this article, the publisher or recipient acknowledges the U.S. Government's right to retain a nonexclusive, royalty-free license in and to any copyright covering the article.

DISTRIBUTION OF THIS DOCUMENT IS UNLIMITED

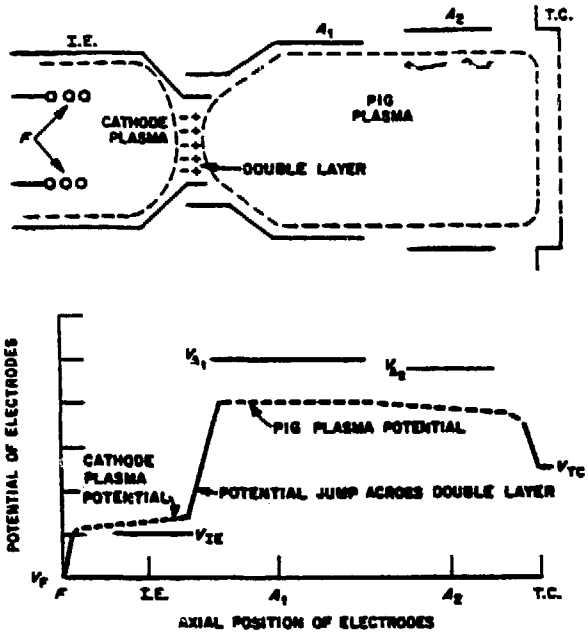

Fig. 2. Axial potential distribution. The symbol T.C. corresponds to the plasma grid in Fig. 1.

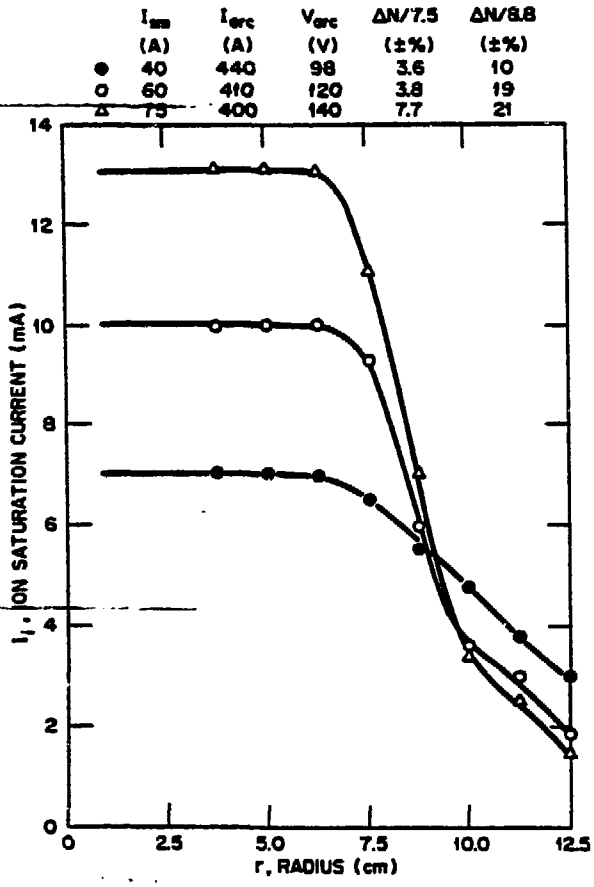

Fig. 3. Density profile for various source magnetic fields (denoted by I_{sm}).

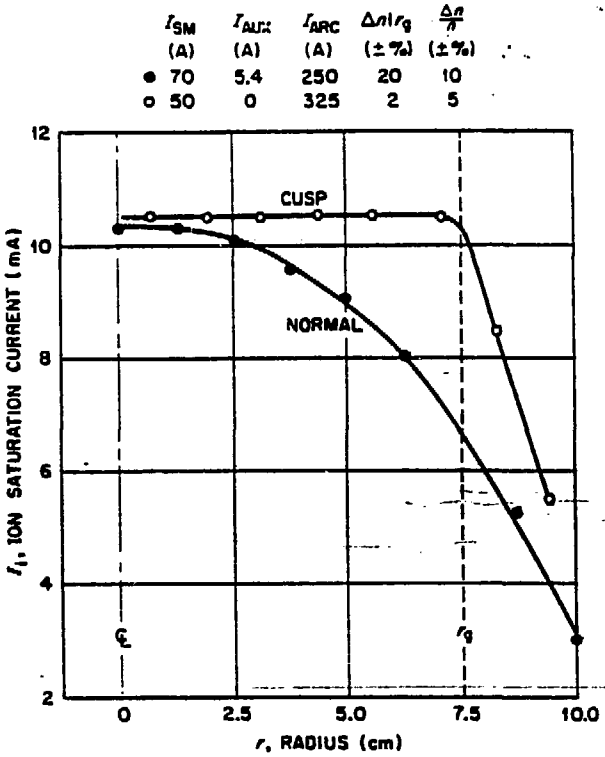

Fig. 4. Typical density profiles with and without axial magnets.

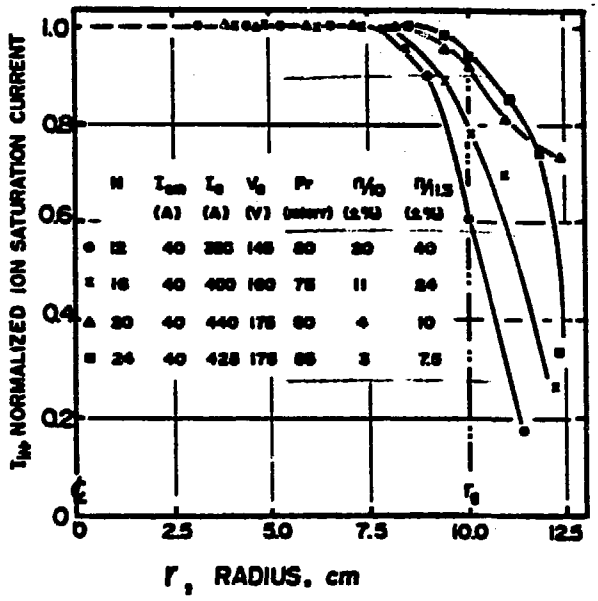

Fig. 5. Variation of plasma uniformity with number of azimuthal magnets.

improved substantially. Thus, a uniform and dense plasma is readily created at a relatively weak axial field (Fig. 4). Moreover, the column number of the permanent magnets affects the plasma uniformity as shown in Fig. 5.

The ionization rate in the anode region usually increases with the gas pressure there. For the 7-cm, 10-cm, and 15-cm grid diameter sources, the pressure increase is obtained by increasing the gas feed into the intermediate electrode chamber. For the 22-cm source, the pressure increase is also controlled by the extra gas feeds into both the anode region and the upper section of the gas cell. Under normal operation of these large sources, the gas feed into the intermediate electrode chamber should be the minimum for reliable operation. The gas feed into the anode region should be adjusted for the desired plasma density or ion beam current density. Then the gas feed into the gas cell is used to provide the desired equilibrium fraction of neutrals in the beam. With the proper arrangement of gas feeds, the source performance is improved, particularly the arc efficiency and monatomic species fraction. With the optimization of gas feed as mentioned above, the source tends to be operated in a high impedance mode, i.e., high arc voltage (greater than 100 V) and low arc current (less than 700 A). However, if the gas feed into the intermediate electrode is too high, the source tends to be operated in a low impedance mode, i.e., low arc voltage (less than 90 V) and high arc current (greater than 900 A). For example, a 60-A ion beam can be formed from an ion source with two different arc conditions: 90 V/900 A and 100 V/600 A.

Hence, the source operated in the high impedance mode is characterized with high arc efficiency, 0.9-A beam current per kilowatt of arc power for this particular case. The best arc efficiency achieved so far is about 1.1 A/kW.

In addition to the optimization of the applied magnetic fields and gas feeds, the optimization of source electrodes is also important for source performance. The electrodes of importance are anode 1, the intermediate electrode, and the hot cathode. They can influence the source reliability and arc efficiency. Arc efficiency, which varies with the dimensions of anode 1, is shown in Fig. 6.

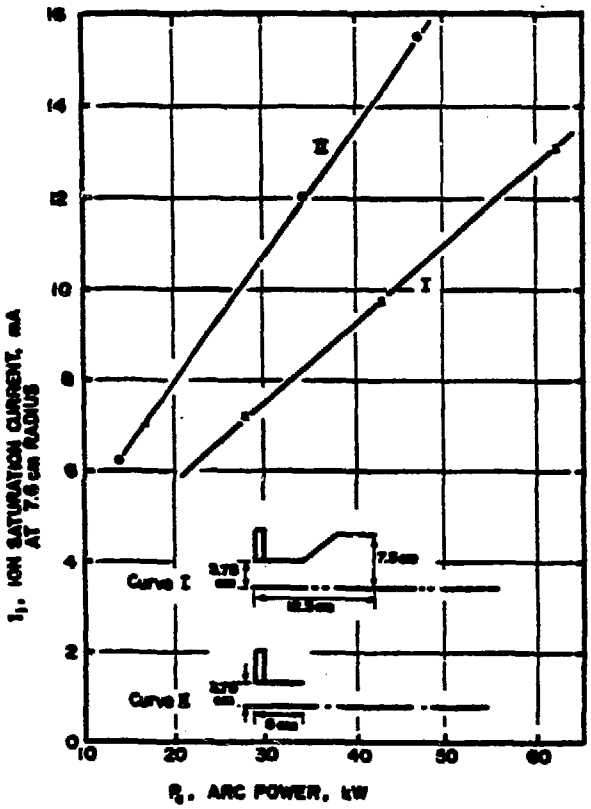

Fig. 6. Variation of ion saturation current with arc power for two types of anode 1.

The optimum shape used in a 22-cm source for PLT injectors is conical. The insert and axial buttons of the intermediate electrode are also optimized for plasma uniformity, source reliability, and high arc efficiency. Figure 7 shows the effect of the button on the uniformity. The filament lifetime problem is reduced by using multiple off-axis filaments in combination with the optimized intermediate electrode. In addition to reducing damage caused by backstreaming ions and electrons, the increase in emission area raises the maximum arc current, stabilizes the double layer, and thus reduces the noise level. For a 7-cm source,[6] the noise level (<10 kHz) is ±30%; for a 10-cm source,[8] the noise level (<10 kHz) is ±5%; for a 22-cm source,[9] the noise level (<10 kHz) is ±3.5% and (<1 MHz) is ±15%.

The 22-cm source for PLT injectors normally operates on the test stand for 100 ms pulses every 10 s. The plasma generator has been reliably run for 500-ms arc pulses for extracting 60 A at 40 kA. A 60-A beam has been extracted for 250 ms at 40 kV. Recently, a 10-cm source for ORMAK injectors has been run for 10-s beam pulses at 6 A/23 kV. In addition to the accelerating grids, the filament lifetime is relevant for long pulse operations. Sources with different electron feeds are being studied and will be reported later. The scalability of the modified duoPIGatron ion source is shown in Fig. 8. There appear to be no physical bounds on source size as yet.

The fraction of monatomic species ions extracted from an ion source is extremely important since molecular species generate gluttonous,[10] undesirable,[11] unrecoverable[12] fractional energy neutrals. They are gluttonous because a disproportionate

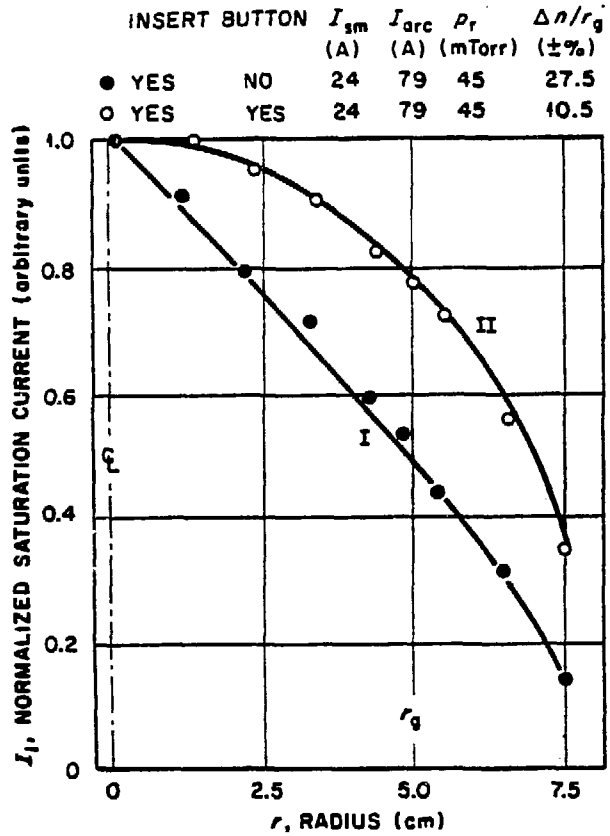

Fig. 7. Typical density profiles with and without utilizing an axial copper button.

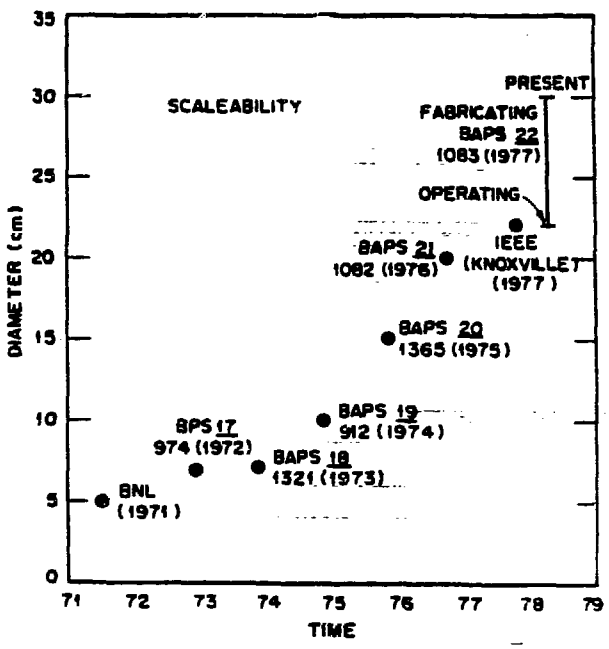

Fig. 8. Illustration of scalability of the ion source.

fraction of neutral power ends up in these low energy components, as described in Sect. 3; they are undesirable because they do not serve to heat the plasma and may even have deleterious effects (Sect. I below); and they are unrecoverable because they are neutral. Monatomic species fractions of 0.50-0.55 were reported on earlier versions of these ion sources.[4-6] Predissociation of the gas before it enters the source and provision of hot walls leads to a significant improvement,[13] as shown in Fig. 9. Hydrogen molecules can be dissociated effectively by passing the gas through a tungsten oven which is at a high temperature (≥2400K). If an equilibrium is established at these high temperatures, about 95% of the gas becomes dissociated through multiple collisions with the hot tungsten surface. Recombination

ORNL DWG 76-12603

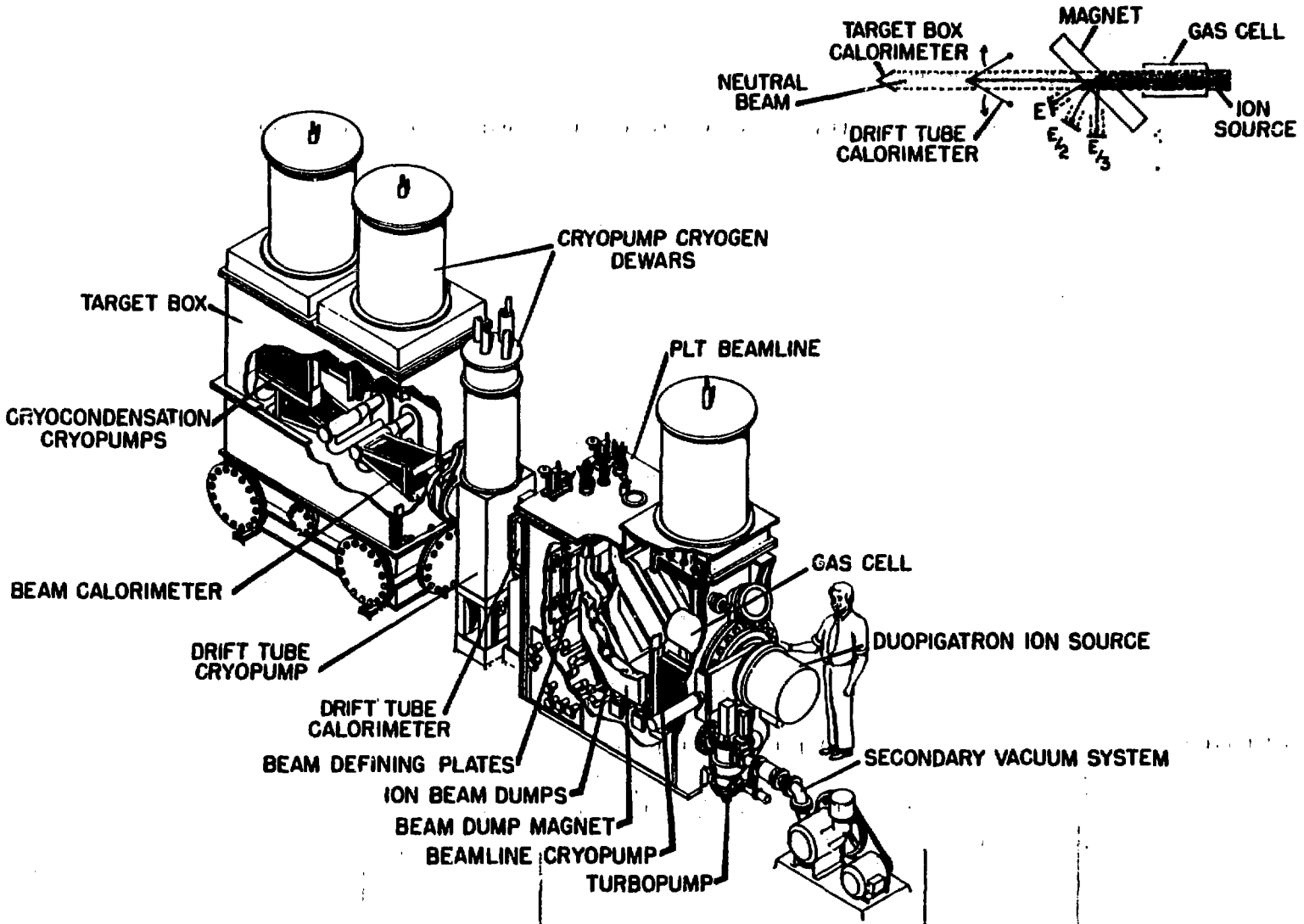

ORNL/PLT BEAMLINE AND ORNL TEST FACILITY TARGET BOX.

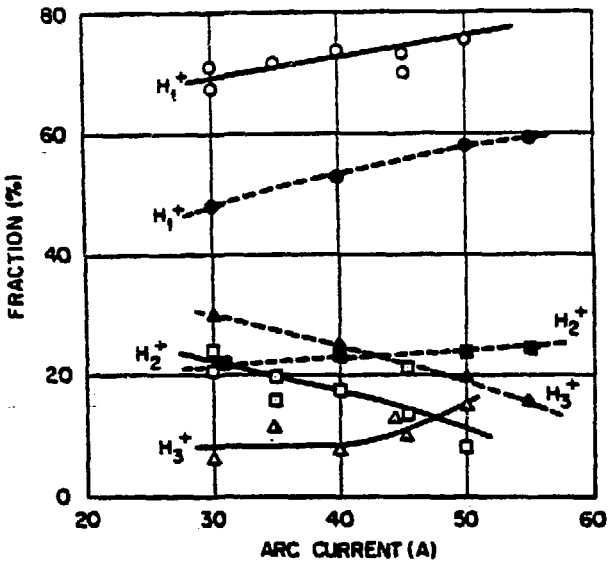

Fig. 9. Ion species distributions at the detector. Open points represent the distributions with predissociation, filled points represent the distributions without predissociation.

due to collisions between particles is expected to be small since the ion source gas pressure is normally low (<0.2 torr). Surface interactions will be a predominant mechanism for the generation of molecular hydrogen. This surface recombination, however, can be reduced considerably by providing hot tungsten walls inside the ion source. In general, desorption of hydrogen from a tungsten surface yields molecular hydrogen if the temperature is below ~1100K. It is therefore desirable to keep the temperature of all the walls above this temperature.

Figure 10 shows a calorimetric scan of the full, half, and one-third energy ion peaks[12] of a 22-cm source without predissociation. This scan was obtained by placing a single 0.6-cm-ID swirl tube calorimeter in the image region of the deflection magnet, as shown in Fig. 11. The three separated ion species were measured as the magnetic field was varied. Figure 12 shows the species ratios as measured at the ion dump and the interpreted species at the ion source and entering the tokamak plasma. The high monatomic yield observed (85%) can probably be attributed to the following: (1) The source with the cusp field arrangement is capable of producing a cold, dense plasma (with low arc power densities) at high gas pressure. (2) Due to the high gas pressure, the primary ionizing electrons can lose enough energy

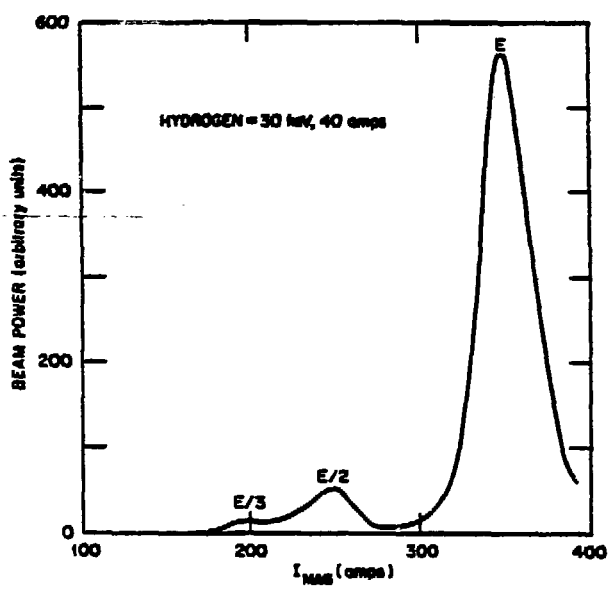

Fig. 10. Calorimetric scan of the full, half, and one-third energy ion peaks from the neutralizer cell.

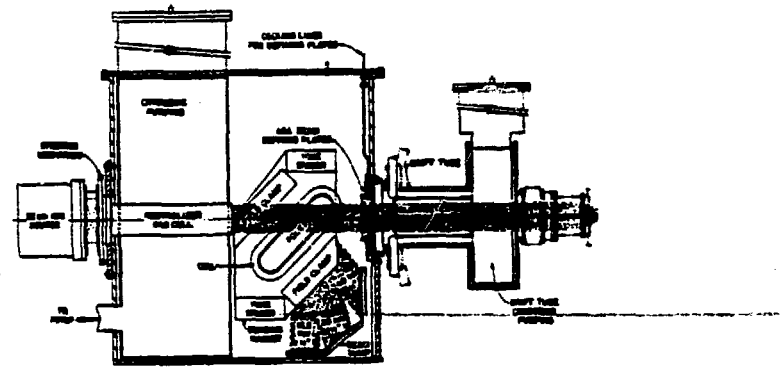

Fig. 11. The MESTF neutral beamline schematic.

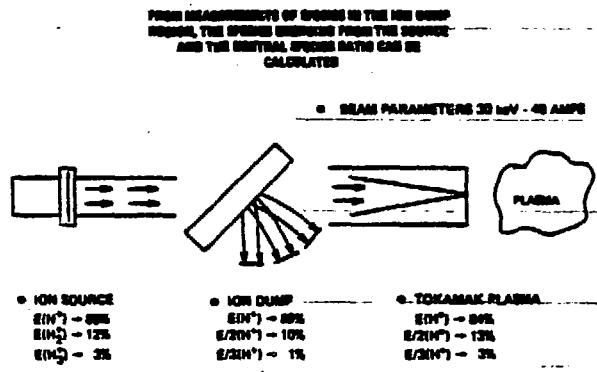

Fig. 12. Measured and calculated species ratio flow chart.

through collisions to fall beneath the ionization threshold energy as they migrate toward the extraction region. Moreover, their density will be too low to create many ions in this region. (3) The cold plasma electrons (≤5 eV) have sufficient energy to dissociate molecular ions and molecules efficiently but have not the energy to ionize them. The electron-molecular ion collision frequency is about 5.6 times higher than the electron-atomic ion collision frequency. (4) The drift velocity of atomic ions is higher than that of molecular ions. Consequently, the ions in the extraction region which make up the beam current are dominated by atomic ions originating in the plasma volume. Applying predissociation to the 22-cm source, as was done for a 10-cm source[13] (see Fig. 9), in combination with providing hot walls may increase the proton fraction further.

The undesirability of a large molecular species fraction is illustrated in the following calculation.[11] It shows that if, for a particular tokamak, the penetration of the full energy beam component is marginal, penetration of the undesirable half energy component is poor and these particles will heat the outside of the plasma. This may be deleterious because a thick, cool edge region prevents energetic particles from hitting the wall. Also, energy deposited near the plasma edge leaves faster and is thus less effective in heating the plasma. To emphasize this point, consider typical 80-keV 85% and 60% atomic yield sources (Table 1). Although the 85% proton source in the example delivers two-thirds the power of the 60% proton source, it is better for heating the center of the plasma since it has more

Table 1

Energy	Percent power	Current into neutralizer	Neutralizer efficiency	Neutral current	Power delivered
85% proton source, 45 A into neutralizer					
80 keV	85%	38.2 A	25%	9.6 A	717 kW
40 keV	10%	9.0 A	60%	5.4 A	216 kW
27 keV	5%	6.75 A	70%	4.7 A	127 kW
60% proton source, 50 A into neutralizer					
80 keV	60%	30.0 A	25%	7.5 A	600 kW
40 keV	30%	30.0 A	60%	18.0 A	720 kW
27 keV	10%	15.0 A	70%	10.5 A	280 kW

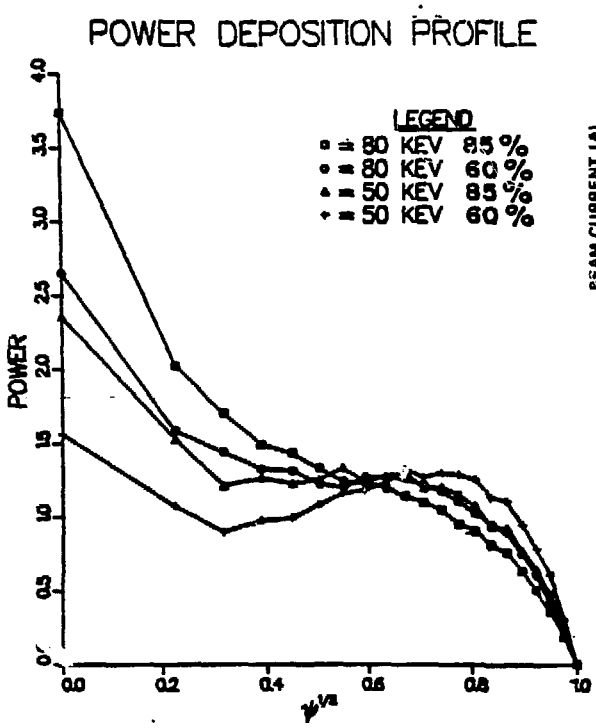

Fig. 13. Beam deposition in Doublet III for the parameters of Table 1, assuming no losses before injection.

power in the high energy component and much less in the two low energy components. The total beam power per unit volume deposition profiles for tangential injection into the top half of Doublet III are shown for four cases in Fig. 13. The innermost point of Fig. 13 is artifically high due to the large (compared to the beam width) size of the first flux surface. The conclusion from this is that it is essential to have a very high atomic hydrogen fraction in the source in order to heat the center of a large dense tokamak.[11]

Another source which has received some attention at this laboratory is the magnetic multipole line-cusp plasma generator.[15-18] The magnetic multipole line-cusp device developed by MacKenzie and associates has been adapted for use as a neutral beam ion source. It has produced high density, large volume, quiescent, uniform hydrogen plasmas. The device is a water-cooled cylindrical copper discharge chamber (25 cm in diameter by 36 cm long) with one end enclosed by a set of extraction grids with a 15-cm-diam multiaperture pattern, as shown in Fig. 14. The chamber wall serves as an anode and is surrounded by an external system of samarium cobalt magnets arranged in a line-cusp geometry of 12 cusps; plasma is produced by electron emission from a hot cathode assembly. This source has achieved extracted beam currents of 14 A at 18.5 kV (see Fig. 15), radial plasma density uniformities of ±5% over a 15-cm diameter, noise levels of less than ±0.5%, and arc efficiencies (beam current/arc power) of 0.6 A/kW.

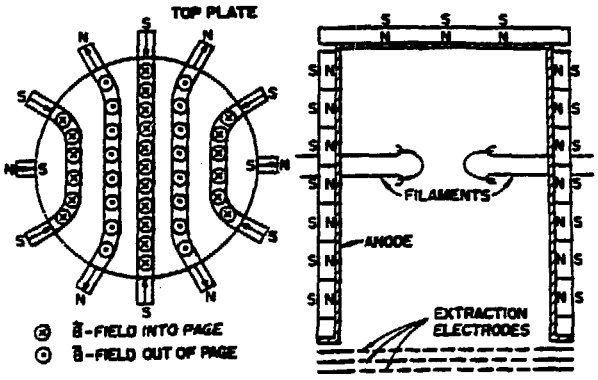

Fig. 14. Schematic of multipole line cusp source.

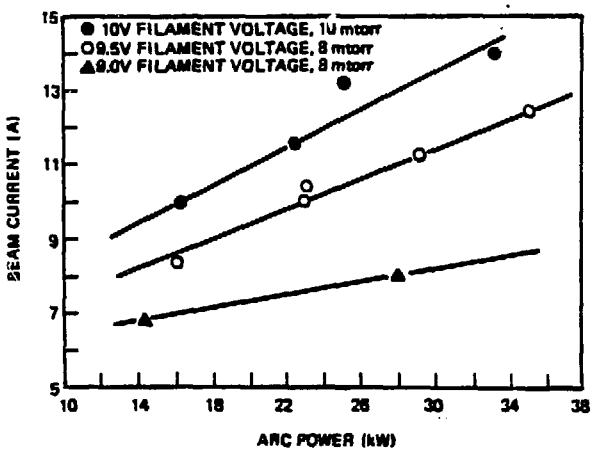

Fig. 15. Extracted beam from multipole line cusp source as a function of arc power and filament voltage.

Another source being considered at this laboratory is a quiescent discharge obtained by replacing the electron feed and cathode plasma region (shown in Fig. 1) with an array of 60 filaments.[19] The source, now under fabrication, is shown in Fig. 16. No attention is given to filament lifetime at this stage of development. Since there is no source magnetic field, this source is expected to be free of noise. In collaboration with D. M. Goebel and A. T. Forrester,[20] a LaB_6 hollow cathode structure was affixed to a 22-cm source, replacing the cathode plasma. Preliminary tests enabled a 30-A ion beam to be extracted. The noise level is approximately ±2%, which is an order of magnitude lower than in a duoPIGatron. Preliminary measurement of the proton fraction of this source was measured to be 90% (the gas flow was three times greater than in the duoPIGatron).

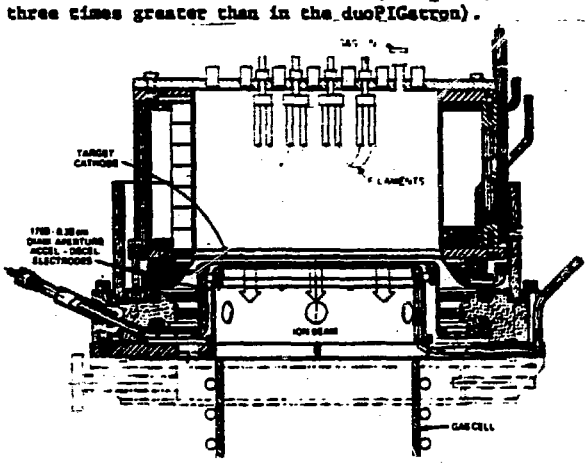

Fig. 16. Quiescent discharge source.

The bottom line for our source development is a duoPIGatron with an 55% proton yield, an arc efficiency of 1.1 A/kW with 65-A extracted current, negligible filament power (81 A/kW), and a nucleon gas efficiency of 60-80% that can be conditioned in less than 50 hr of operating time with a duty cycle of 1%. Such sources have been used on ORMAK and PLT injectors and will probably be used on ISX and PDX injectors.

2. ION OPTICS AND ACCELERATING STRUCTURES

We describe some theoretical methods and developments pertaining to ion optics, the associated experimental methods and developments, and an examination of accelerating structures. A two-dimensional solution was found to the Poisson-Vlasov equation for ions extracted from a collisionless plasma with a Boltzmann electron distribution.[21] Poisson's equation is solved by a finite difference method on a mesh with given source terms, using the method of successive overrelaxation (SOR). Boundaries are treated with a procedure due to Hornsby.[22] The overrelaxation coefficient is automatically chosen using a method due to Carré for the maximum rate of convergence. A stretched grid in the axial direction is chosen such

that mesh points near the emitter are relatively close together. Vlasov's equation is solved indirectly by solution of orbit equations for many initial orbits entering from the emitting surface toward the hole with velocities appropriate to the initial velocity distribution specified. After consideration of electric fields produced by the solution of the Poisson equation and centripetal forces, the orbit equations are solved by a deferred limit integrator and ion charge is deposited on the mesh points in accordance with the continuity equation.

Electron charge is deposited directly on the mesh points by iterating and underrelaxing as suggested by W. S. Cooper[23] (denoted by A in Fig. 17), until a solution is reached. Ions are iterated after a solution is found for a previous iteration. An illustration of the ion iteration scheme is shown in Fig. 18 where the top part shows the ion trajectories through the vacuum solution and the bottom shows the converged solution to the Poisson-Vlasov equation. A

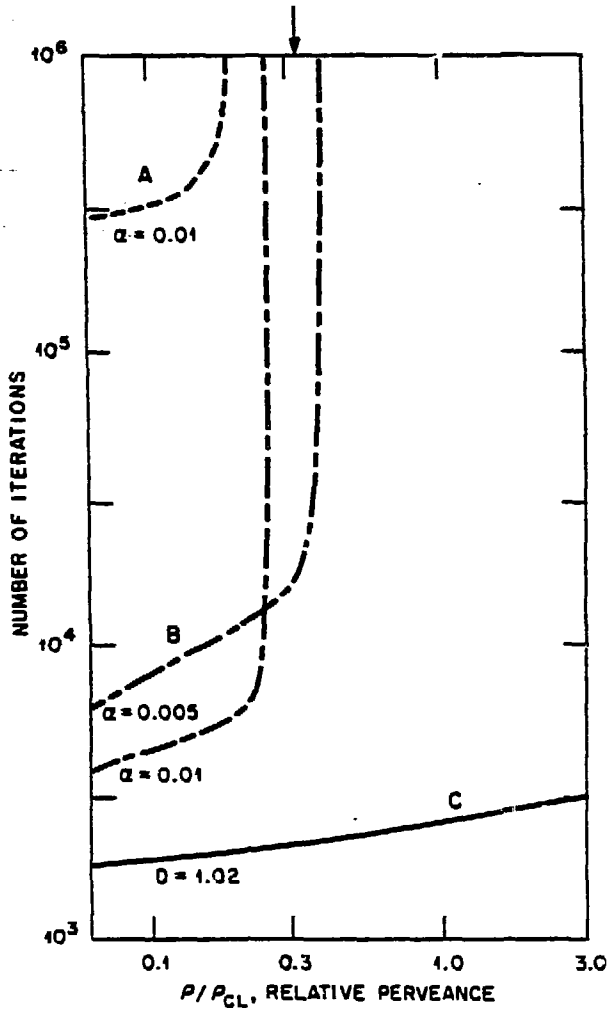

Fig. 17. Comparison of computational time for the three schemes considered as a function of perveance on the scale of the Child-Langmuir perveance. The arrow on the abscissa is the perveance where the ion beam is most convergent.

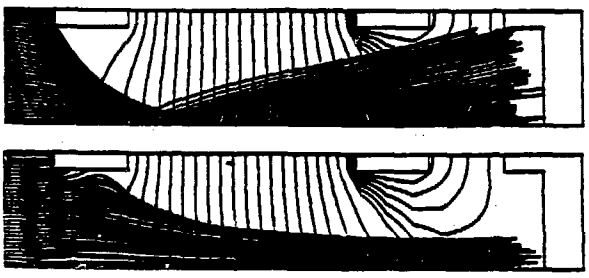

Fig. 18. Typical converged solution (bottom) and initial iteration in vacuum fields (top) at a relative perveance of 1/3.

more expeditious iteration scheme[24] was found by not requiring a solution before iterating the electrons (denoted by B in Fig. 17). A yet more expeditious iteration[24] was found by accelerating the underrelaxation as well (denoted by C in Fig. 17 and by method I in Fig. 19). From Fig. 17 we see that convergence problems are eliminated with scheme C, at least in the sense of numerical stability. It should not be inferred that the iteration scheme used by W. S. Cooper is as inefficient as Fig. 17 suggests (scheme A), because we were using an iterative solution to the Poisson equation and a single precision IBM machine. (The powerful mesh generator was developed by Hornsby and was written with many overlays which make it nontrivial to convert to double precision.) Cooper does not use an iterative scheme and uses double precision. This could significantly change the radius of convergence of the solution and its efficiency. A yet more expeditious and accurate scheme was developed[25] which put the electrons implicitly into the linear SOR solution. This Newton SOR iteration has provable uniqueness and convergence properties. Shown in Fig. 19 is a comparison of the computational effort for the accelerated underrelaxation scheme and the Newton SOR scheme as a function of the maximum accuracy of the solution and mesh size. We had to teach the IBM 370/195 to do the exponential in an expeditious manner, saving a factor of 15 in the exponential calculation and a factor of three in the entire code.[26] With this apparatus we were able to do several comprehensive studies.

The best scheme of Ref. 24 was used to examine the effect of plasma properties on ion optics.[27] This was the first time the ion extraction solution was carried back far into the source plasma (100 Debye lengths, as in Fig. 18). Ion optics is always found to be dominated by aberrations for thick cylindrical bore apertures, with the ion temperature playing a minor role and the electron temperature playing virtually no role. An important effect of ion temperature is that the optimum perveance decreases as the ion temperature increases. The more accurate Newton SOR scheme[25] shows the same results.[28] The perveance at which a solution can be obtained is indefinite, extending at least far beyond the Child-Langmuir space charge limited flow. The electrons in the plasma prevent space charge limited flow no matter what the source plasma density. We used the Newton SOR scheme[25] in the following studies.

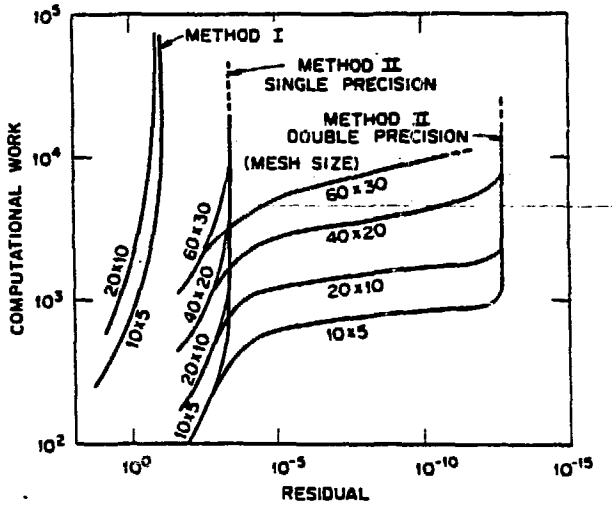

Fig. 19. Properties of the accelerated underrelaxation scheme (Method I) compared to the Newton SOR iteration scheme (Method II).

Several different shaped aperture plasma grids were studied, yielding the well known conclusion that a pseudo-Pierce shape virtually eliminates the aberrations but decreases the optimum perveance.[29] Emittance diagrams for a cylinder bore and for a pseudo-Pierce geometry are shown in Figs. 20 and 21, respectively. Orbit trajectories for the pseudo-Pierce geometry are shown in Fig. 22.

A study of tetrode optics with cylindrical bore apertures was made[30] (see Fig. 23 for a typical trajectory computation). The principal conclusion is that if the field ratio between gaps can be suitably

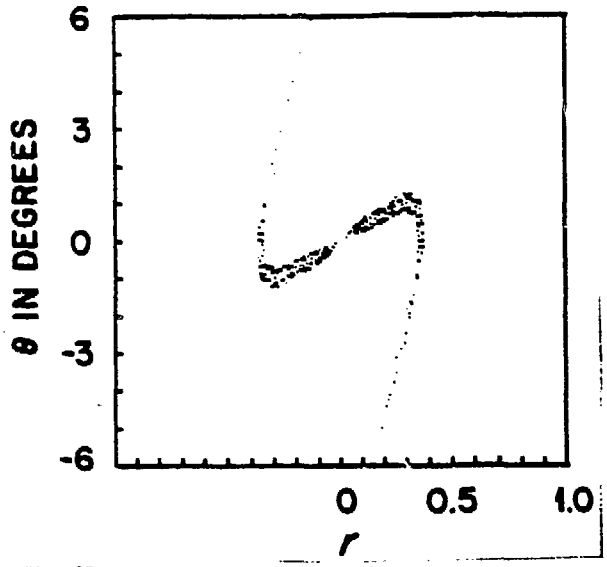

Fig. 20. Emittance diagram of cylinder bore aperture.

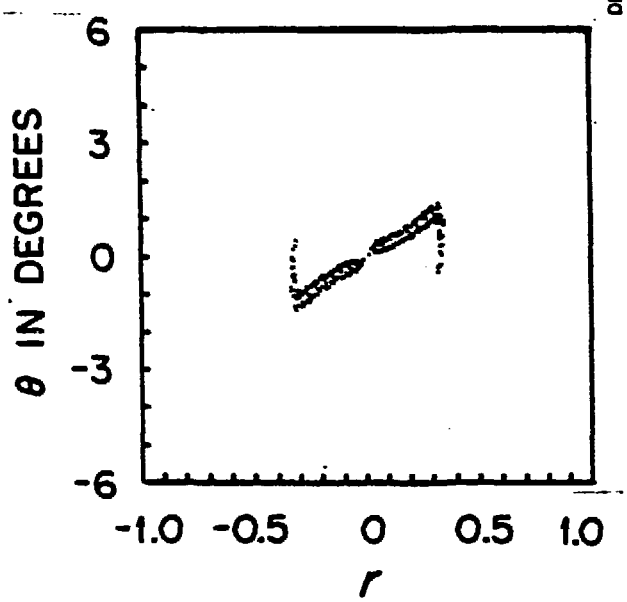

Fig. 21. Emittance diagram of pseudo-Pierce apertures.

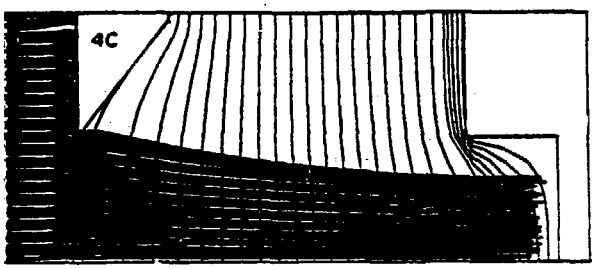

Fig. 22. Orbits in converged solution for pseudo-Pierce geometry at optimum perveance.

adjusted, the aberrations of the plasma electrode can be minimized at optimized perveance since in this case the source plasma is pushed far into the aperture. The manifestations of this are illustrated in Fig. 24. This conclusion is not relevant to aperture shapes which cause little aberration. Also, the sensitivity to source density variations is smaller in the tetrode than in a cylindrical bore triode of the same gap as the tetrode extraction gap. The absorption of plasma ions into the plasma electrode is far larger for the tetrode than for the triode under normal operating conditions, yielding a relatively low optimum perveance.

Fig. 23. Orbits in converged solution for tetrode.

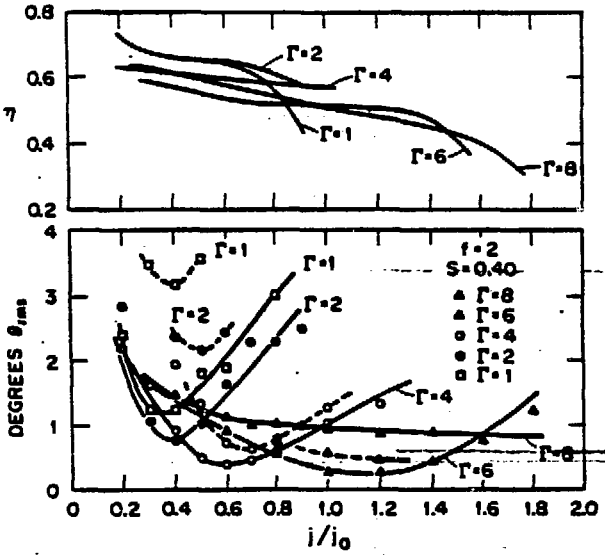

Fig. 24. Total rms divergence (dashed) and truncated distribution divergence and transmission efficiency, η, as a function of perveance and potential distribution for a tetrode.

The effect on ion optics of a preacceleration potential applied to the plasma electrode was studied.[31] A principal result is that the ion divergence is decreased as the preacceleration potential, μ, is raised, as shown in Fig. 25. Figure 26 shows an emittance diagram for a large preacceleration potential of μ = 0.1. The electrical connections are shown in Fig. 1. An insulator on the plasma side of the plasma grid shows the same effect with the application of a precel potential. This theoretical result predicted all of the subsequent experimental findings, adding new dimensions to the applicability of the ion optics code to the real world.

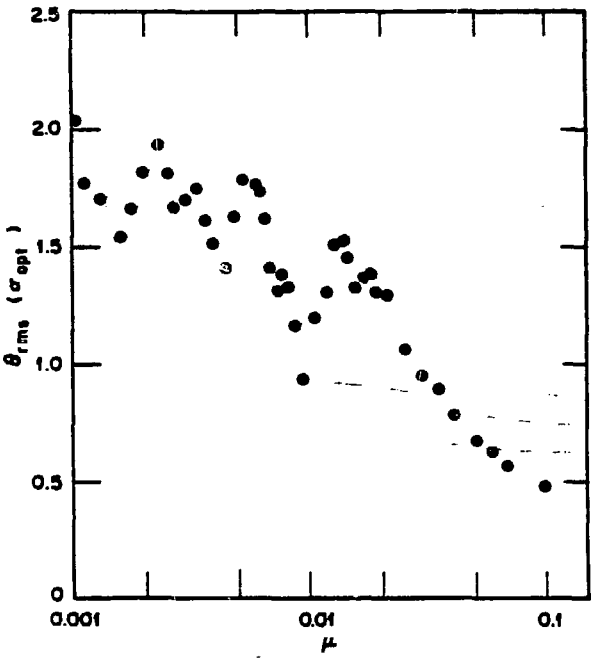

Fig. 25. The rms beamlet divergence as a function of precel potential, on the scale of the accel potential, μ, at optimum perveance. The left-hand side of the graph corresponds to and isolated conductor.

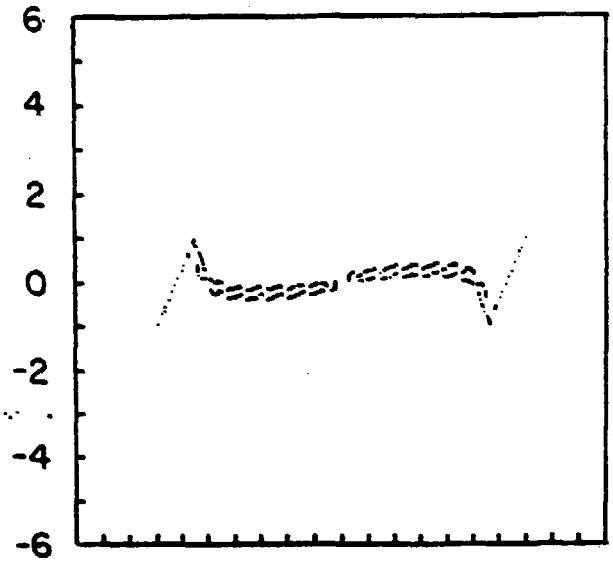

Fig. 26. Emittance diagram of a cylindrical bore aperture plasma grid at a precel = 0.1 accel.

By reversing the polarity of the potential on the plasma electrode from that in the precel case, a limiting singular solution to the Poisson-Vlasov equation is approached as the plasma electrode potential equals the plasma potential. It is characterized by no aberrations, no absorption by the plasma electrode (even though it is cylindrically bored), and a great sensitivity to noise or plasma variations. An emittance diagram for this case is shown in Fig. 27.

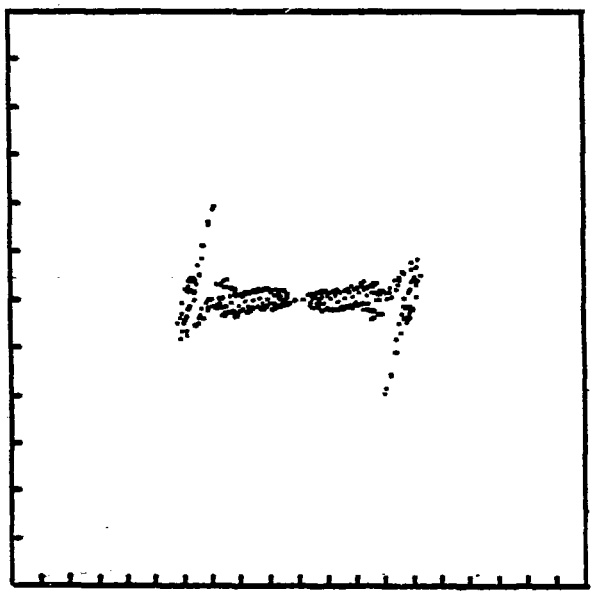

Fig. 27. Emittance diagram of a cylindrical bore aperture plasma grid at a potential equal to about the plasma potential.

The effect of plasma density variation on ion optics was studied for triodes with various shaped holes, aspect ratios, and preacceleration potentials, as well as for tetrodes.[3] A principal result was that for large aspect ratios the sensitivity to optimum perveance increases substantially. The aberrations do not noticeably increase with large aspect ratio,[28] leading to the conclusion that noise or inhomogeneous plasma density is the cause of the well-founded experimental observation with noisy sources that large aspect ratios cause poor optics. This suggests the extent to which the source plasma is uniform. The low noise sources described in Sect. 1 above should not show a deterioration of optics with large aspect ratio (see Fig. 28), as found in the Culham studies.[32] This would ease some constraints on source design.

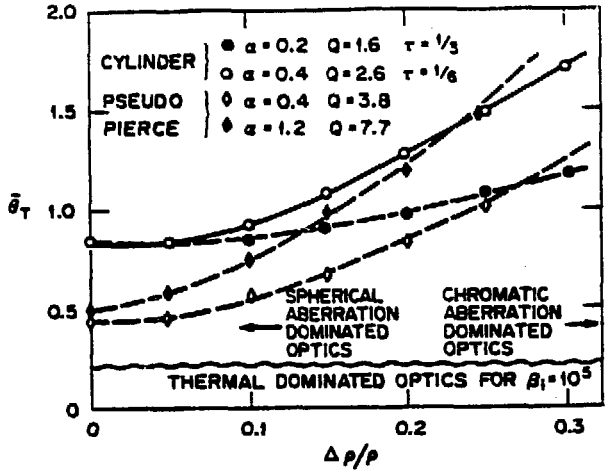

Fig. 28. Variation of divergence angle with density fluctuations for four cases.

Noise in the source plasma may cause the effective ion temperature to be higher than it would be without the noise. This is because the ions are pushed around by the grossly fluctuating local fields before they are extracted. Thus, the optimum perveance will be higher for a noisefree source than for a noisy source in view of the analysis of the effect of source ion random motion.[27,28]

The effect of aperture displacement on steering in tetrodes has been computed,[33] predicting that the steering is a function of the field ratio between the gaps. An elaboration of the computation caused improvement in the accuracy.[34] A computation[35] of beamlet-beamlet interaction in the acceleration region, suitably elaborated,[36] shows that for aberration dominated optical systems such interactions are negligible, but they may be significant for emittance dominated optical systems.

Experimental optics studies fall into two classes: measurement of single beamlet intensity distribution and measurement of a multibeamlet source power deposition. A single beamlet study was done for a variety of shaped plasma apertures.[29] For a pseudo-Pierce shaped electrode, the half-width half-maximum (HWHM) beamlet divergence angle was 0.6°. For a cylindrical bore aperture the HWHM angle is 1.0°. This improvement is in agreement with the theoretical results.[29] A movable Faraday cup placed 1 m from the acceleration electrodes was used, and the accelerating potential was approximately 24 kV. The optimum perveance was thought to decrease for the shaped electrode, in accordance with the theoretical results. However, the fraction of drain current due to the beam in single beamlet studies is uncertain due to the possibility of plasma leakage to the gas pumping hole in the electrodes.

A single beamlet study of the tetrode was preformed.[30] A principal result is that for a high ratio of second gap to first gap fields the ion optics improves considerably. This is in agreement with the theoretical results.[30] These studies were done up to 60 kV. Further single beamlet studies were done from 60 kV to 110 kV.[37] The optimum perveance is far lower than that indicated in the lower energy studies and by the paraxial studies,[30] but is in agreement with the computational results if the absorption of the ions into the plasma electrode is taken into account (see Fig. 7 of Ref. 30). In the lower energy study the minimum beam divergence (HWHM) was 0.4° at 60 kV (Ref. 30) and in the higher energy study the minimum beam divergence (HWHM) is 0.25° at 100 kV.[37]

A single beamlet study on the effect of preacceleration with insulator coating was performed.[31] A 0.02-cm-thick coating of aluminum oxide was deposited, by the plasma spray technique, on the side of the plasma electrode facing the source plasma. With a movable Faraday cup positioned 1 m from the acceleration electrodes, a θ_{HWHM} as low as 0.55° was measured for an accel potential of 14.4 kV, a precel potential of 0.32 kV, and an accel gap of 0.56 cm (see Fig. 29). With an accel gap of 1.4 cm, a divergence angle θ_{HWHM} of 0.31° was measured at an accel potential of 28.5 kV and a precel of 0.49 kV.

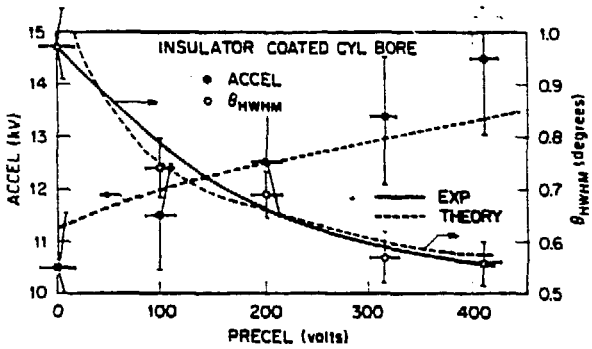

Fig. 29. Minimum divergence angle as a function of precel potential. Also shown is the accel potential for minimum divergence.

This is the smallest HWHM divergence angle we have ever observed at these relatively low voltages.

The steering properties of tetrodes[34] and triodes[38] were experimentally determined and the theoretical prediction[33] that tetrode steering was dependent on the fields in the gaps was borne out. In addition, the tetrode steering was observed to be extremely nonlinear,[34] even for relatively small displacements. This is attributed to the small aspect ratio and was not predicted by the linear analysis.[33]

All of the previously mentioned single beamlet experiments measured beam distributions using a moveble Faraday cup. For the measurement of transmission and deposition properties and beam distribution of multibeamlet sources, several other diagnostics were developed. An on-line optical diagnostic of neutral beam distributions is being developed[39] which measures excitation light from parallel chords of a beam cross section by an array of PIN photodiodes. This information can in principle be unfolded by an Abel inversion to yield beam distributions. The pinhole camera is another diagnostic used to examine beam distributions. A small aperture (1/32-in.) is placed in the center of a water-cooled target at the focal plane to which the beamlets are steered. A sheet of Mylar is placed behind this small aperture. An image of the aperture grids is produced which shows the contribution from each beamlet.[40] This diagnostic gives information about the plasma density, uniformity, and electrode shape. It can, with considerable elaboration, give information on beamlet distributions while the source is operating.[40] An array of pyroelectric disks has also been utilized to measure ion and neutral beam distributions.[41] The response of these disks is sufficiently fast to examine the beam distribution within a pulse. Finally, measurement of power deposition comes from determination of water flow rates and temperature rise at virtually all places where beam interception is possible (e.g., grids, gas cell, beam dumps, target). A PDP 11/40 computer gives on-line determination of power deposition which accounts for over 95% of the input power.[14]

A typical power deposition profile as a function of perveance is shown in Fig. 30. A most interesting

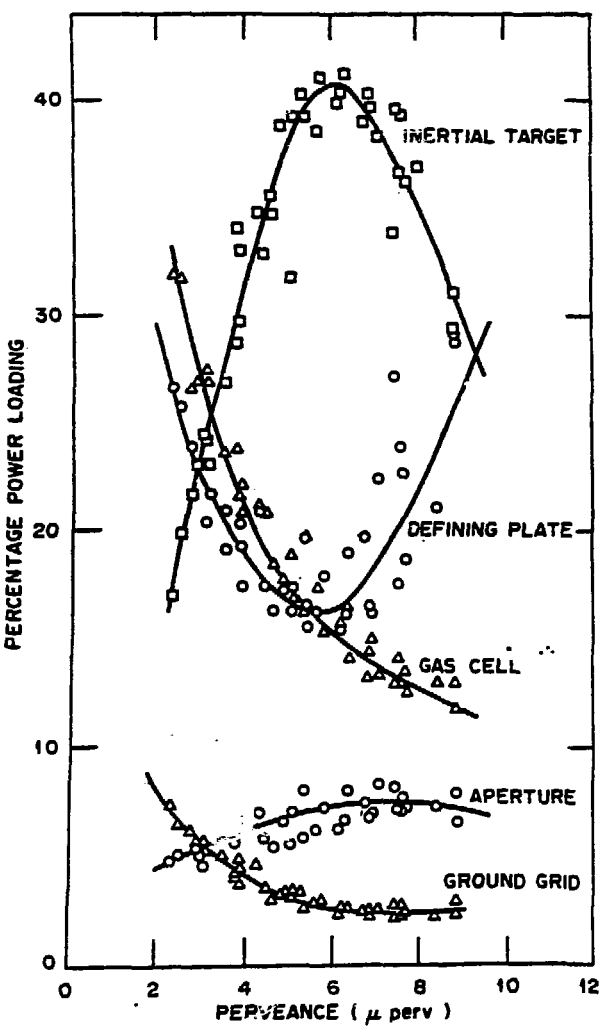

Fig. 30. Power deposition for cylinder bore electrode as a function of beam perveance.

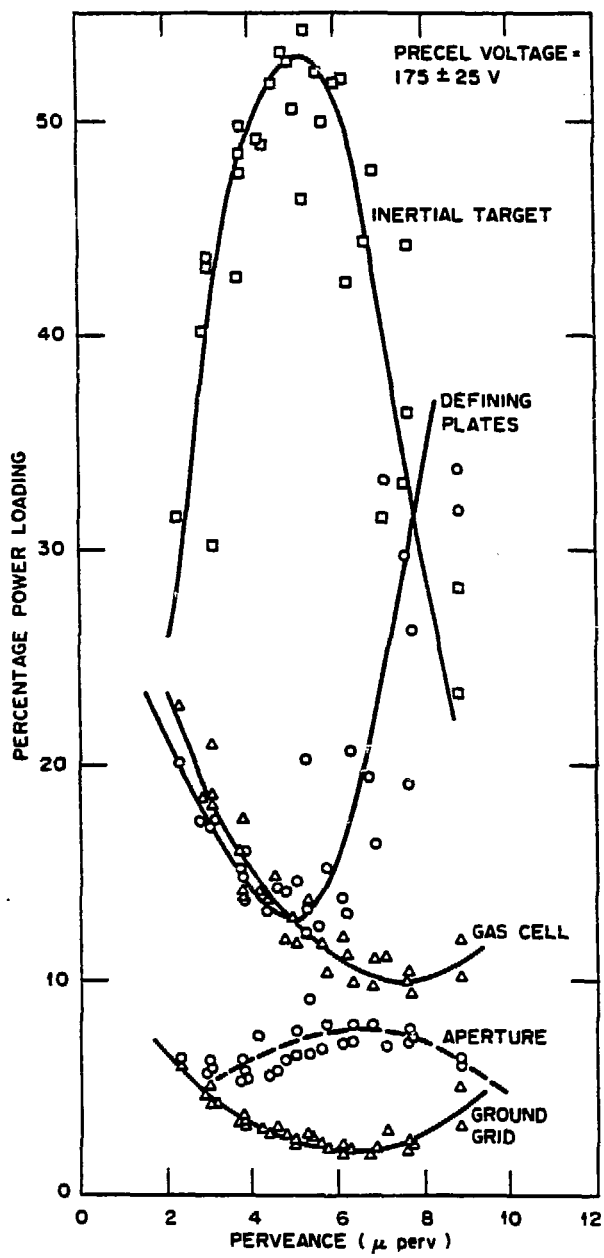

Fig. 31. Power deposition as in Fig. 30 but with 180-V precel.

feature of Fig. 30 is the large fraction which hits the gas cell wall and beam defining aperture.[42] This is not consistent with beamlet profiles which are Gaussian[43] but is consistent with a Lorentzian beamlet distribution.[44] The more sophisticated computations[21-31] more accurately described the situation where the computed[28] perveance dependent beam distributions are in agreement with the differing optimum perveance found on the various curves in Fig. 30. The addition of a precel[31,45] improves the power on target as shown in Fig. 31. A virtue of the precel technique is that by connecting the plasma electrode to either the arc negative or intermediate electrode, the optics may be improved. This technique has been used on existing PLT neutral injectors with benefit. Transmission measurements for a shaped plasma electrode[46] are shown in Fig. 32. Since the transmission is higher than that of a cylinder bore aperture electrode, and an applied precel also increases the transmission of a cylinder bore electrode, by inference it is expected that the addition of a precel to a shaped aperture electrode will increase the transmission still further.

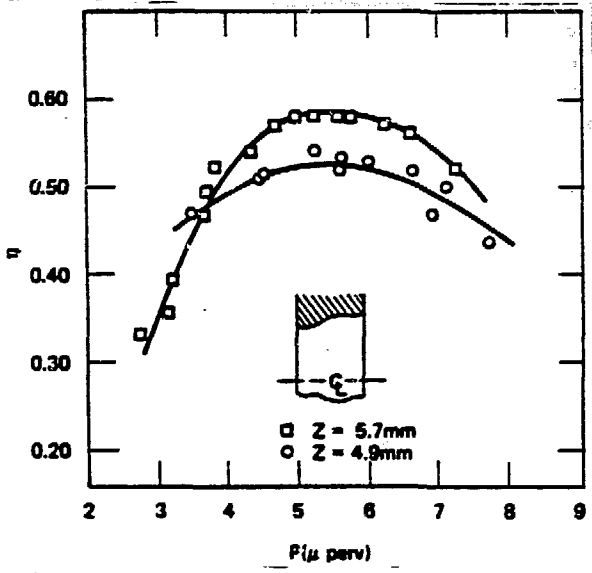

Fig. 32. Transmission efficiency to a 1.8° target for shaped cylinder bore aperture plasma electrode as a function of perveance and accel gap, Z, for voltages up to 40 kV.

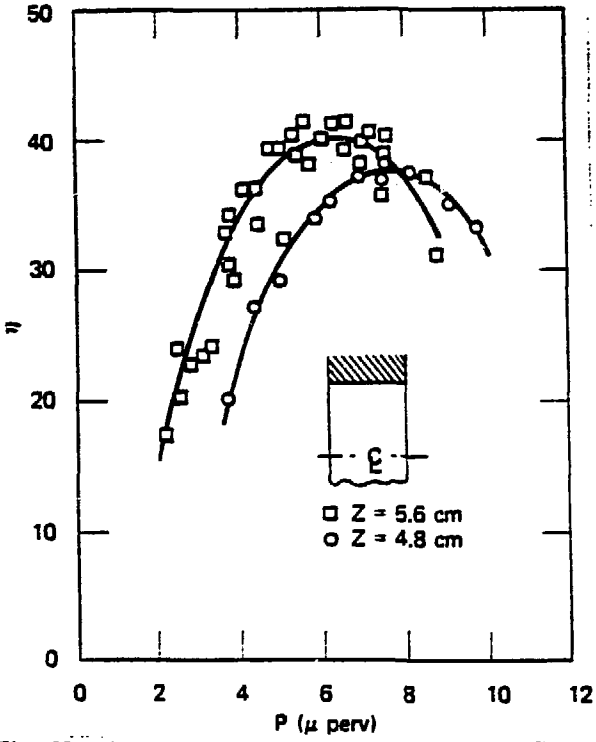

Fig. 33. Transmission efficiency to a 1.3° target for cylinder bore aperture plasma electrode as a function of perveance and accel gap, Z, for voltages up to 40 kV.

The effect of gap spacing on shaped electrodes and cylinder bore electrodes is shown in Figs. 32 and 33, respectively.[46] As the accel gap decreases, the transmission efficiency decreases. Theoretical evidence suggests the sensitivity to nonoptimum plasma density explains this.[9] Pinhole camera results for the larger and smaller gaps shown in Fig. 32 are shown in Figs. 34 and 35, respectively.

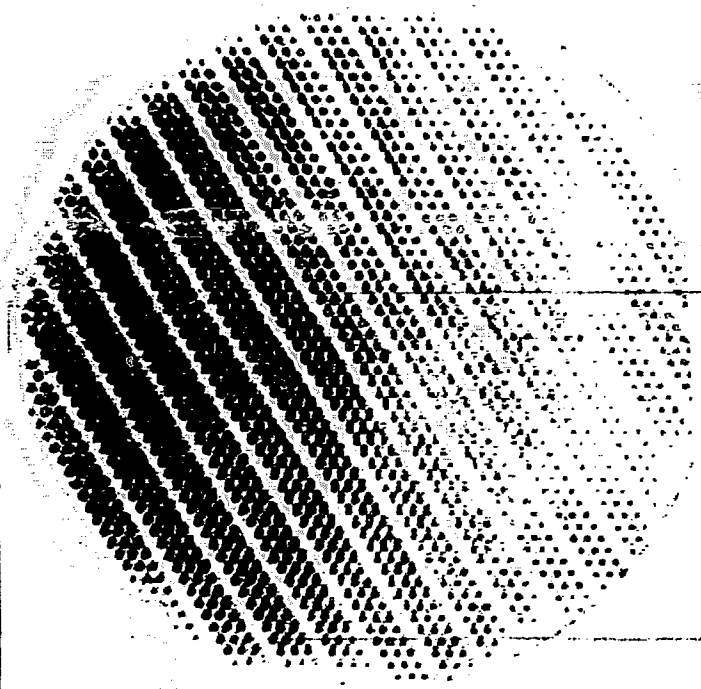

Fig. 34. Pinhole camera result for the case shown in Fig. 32 with Z = 5.7 cm.

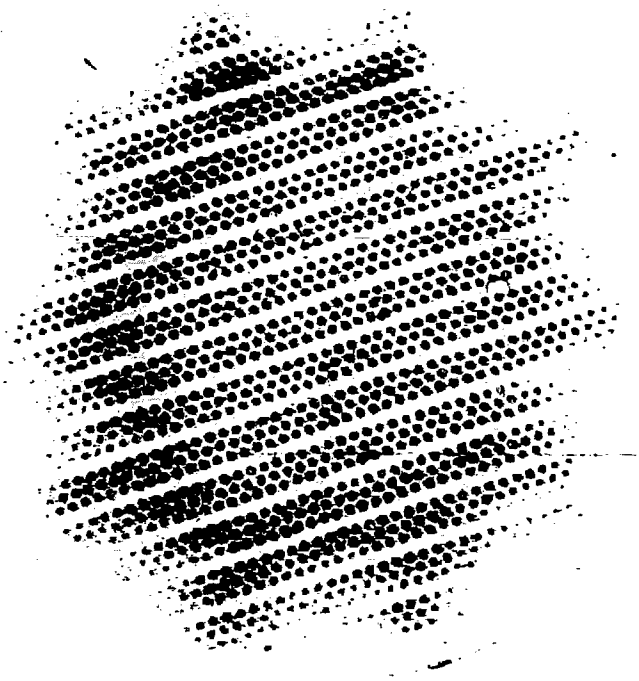

Fig. 35. Pinhole camera result for the case shown in Fig. 32 with Z = 4.9 cm.

The cusped pattern shown in Fig. 35 indicates plasma density inhomogeneities due to the cusp fields. This should be present also in Fig. 34 but the insensitivity to such variations[9] due to the large gap hides the feature. The effect of noise on ion optics is hinted at in Fig. 36, where a relatively noisy duoPIGatron ($\Delta n/n \sim \pm 0.15$) is compared with a $LaBr_5$ hollow cathode source ($\Delta n/n < \pm 0.02$) (the electrodes were misaligned in both studies). The optimum perveance appears higher with the quieter source, as predicted by the theoretical results[27,28] coupled with the hypothesis of fluctuation enhanced ion temperature as mentioned above.

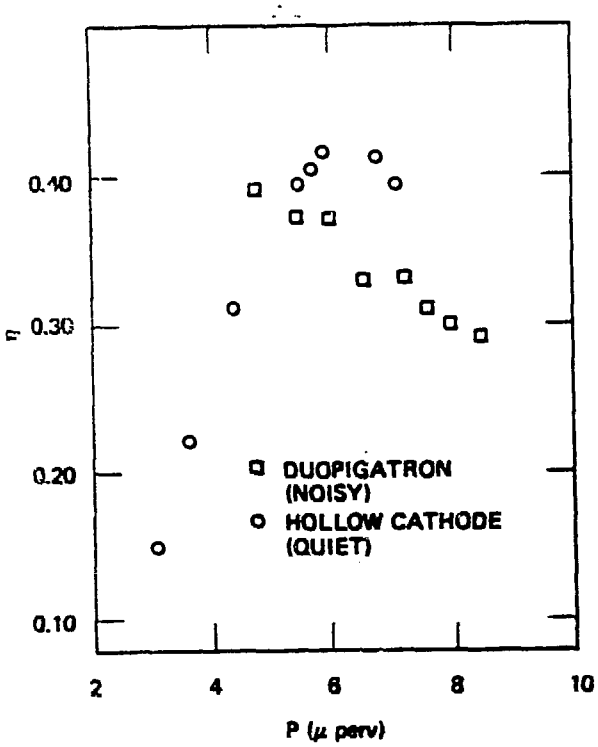

Fig. 36. (a) Transmission efficiency as a function of source noise and perveance. (b) Power deposition for a multiaperture tetrode as a function of perveance.

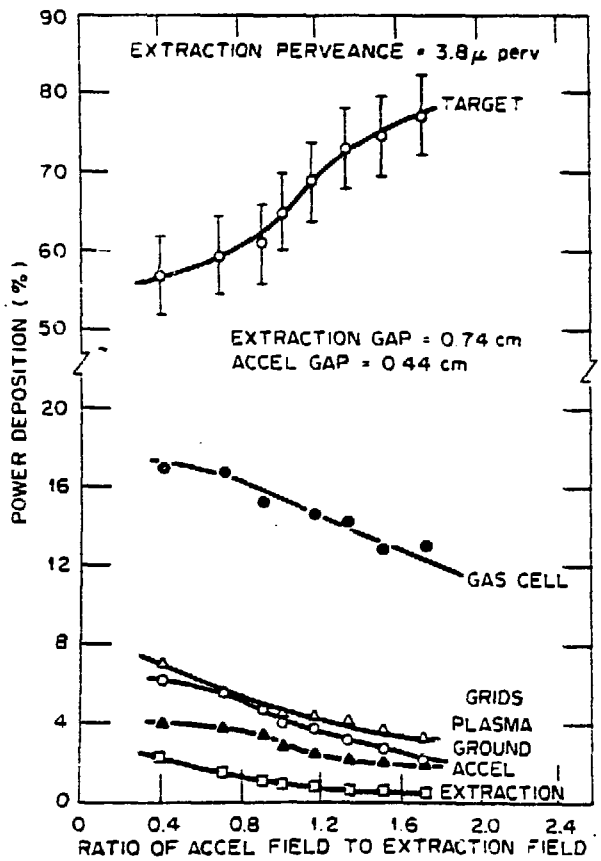

Fig. 37. Power deposition for a multiaperture tetrode as a function of gap field ratio at fixed perveance.

We have developed a high energy test facility for sources using two-stage accelerating structures. Using 1-cm extraction and accel gaps, hydrogen beam energies of up to 104 kV at 10 A have been attained. Using a source with a 0.75-cm extraction gap and a 0.45-cm accel gap, the characteristics of a two-stage multiaperture source (18-cm grid pattern) were studied over the wide range of perveances and accel/extraction field ratios, as shown in Fig. 37 (total energy, 38-58 keV, all at 15 A). The transmission efficiency was found to be a strong function of the accel/extraction field ratio as predicted by earlier measurements and theoretical results.[30,37] A transmission efficiency of (83 ± 5)% of the beam was achieved on a target subtending 2.0° and located 4 m away. This study is consistent with the 0.30° HWHM single beamlet divergence studies[37] in the same way that the single stage 40% target deposition is consistent with the 1.0° HWHM single beamlet studies. Unlike single stage sources, the two-stage source could also be operated with the plasma generator turned on prior to establishing the accelerating electrode potentials.

The design of grid structures as indicated above is dominated by beam optics and transmission. However, other elements of electrode design are important as described below. The principal limitation on steady-state operation of these sources is probably the need for the electrodes to operate normally without melting, distortion, or other deterioration. A grid design which is often used (illustrated in Fig. 38) has water-cooling channels which minimize these problems. The electrodes are fabricated from 3/32-in.-thick copper with 1/16-in. copper tubing furnace brazed into machined channels. Other materials such as molybdenum, tungsten, and tantalum have been considered. However, the difficulties with fabrication are considerable. Construction methods being pursued are furnace brazing of slabs of molybdenum or copper with machined cooling channels, heavy plating of copper slabs with machined cooling grooves filled with a removable "wax" or etchable metal, and a one piece sintered molybdenum construction. A one-dimensional approximate solution to the heat conduction equation was used[47] to estimate heating characteristics and showed that under typical circumstances the copper temperature reached 50% of its melting point. For a 22-cm source grid, distortion and/or warping are hinted at in Fig. 34.

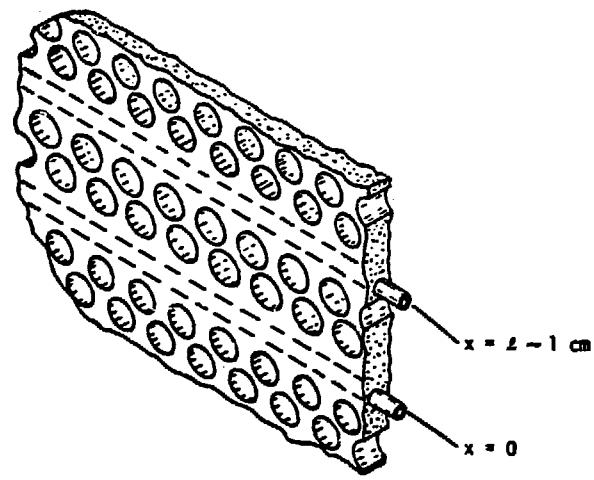

Apertures 2 mm radius

Grid Thickness 1.5 - 2 mm

Local Transparency, T = 65%

Fig. 38. Typical electrode design.

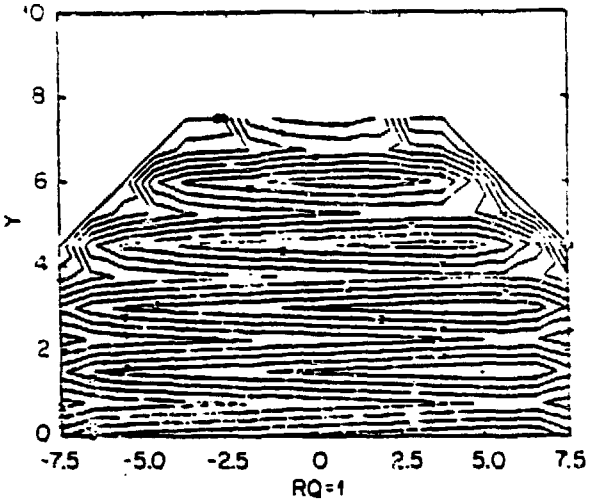

Fig. 39. Two-dimensional temperature distribution of an electrode with water lines.

A two-dimensional heat conduction calculation was carried out[48] explicitly including the water lines. An example of the results obtainable is shown in Fig. 39, displaying the temperature distribution of a copper electrode with water lines.

Other considerations include electrostatic deflection[49] which could be serious for large electrodes, voltage holding criteria for tetrodes,[50] elimination of the third electrode in a triode by insulator coating, and voltage application.[51] A theoretical study comparing the properties of slots and hole multiple aperture electrode structures is under way.[52] Principal properties considered are aberrations, sensitivity to density variations, and transmission. Slots previously[53] considered at this laboratory were fabricated from a milled copper plate. For a noisy source, slots gave relatively high ion divergence. Now that the sources are quieter, we have considered design of steady-state, easily fabricated, deflectionless, high transmission tubes.[54] The idea is to stress the tubes while water-cooling them. Thermal prestressing was rejected due to thermal creep, but spring stressing appears attractive. Such tubes fabricated from work-hardened, 0.082-in.-diam, 0.009-in.-thick stainless steel 304 have been tested for deflection and loading capacity. Using an oxyacetylene torch in contact with the surface, the slot was found to show no deflection ($<10^{-4}$ in.) with about 200 lb stress and 30 cm^3/sec water flow. Power loading was tested ohmically and showed that power densities of greater than 1.4 kW/cm^2 could be absorbed at steady state (>3 min).

The bottom line of our study of ion optics is that we have invented and utilized several methods for increasing beam transmission efficiency. However, we are not yet absolutely sure what mechanisms are dominant in the remaining inefficiency. The prime suspects on the 22-cm source, as evidence above suggests, are: (a) plasma electrode induced beamlet aberrations, (b) misaligned or warped electrodes, (c) source plasma inhomogeneity or fluctuations, and (d) noise induced anomalous ion temperature. Less likely suspects are: (a) normal ion temperature, (b) residual space charge blowup in the neutralizer cell, and (c) beamlet-beamlet interaction in the acceleration gap.

3. BEAM LINE DESIGN/SYSTEM ENGINEERING

Principal items in the design of a neutral beamline not included above are: (a) power supplies and control for the ion source and accelerator, (b) vacuum systems, (c) neutralizer cell, (d) direct recovery, (e) drift tube, and (f) target design. These items are included in this section.

There are at least seven power supplies necessary for source operation. The biggest power supply is that which accelerates the ions. The following describes the function and performance of a fast series switch between this high voltage power supply and the accelerating structure of the ion beam accelerator used in high power neutral beam injection systems.[55]

High voltage breakdown in the accelerating structure of a high power ion beam accelerator is initially frequent and finally occasional or even rare as the structure reaches what is commonly called the "conditioned" state. This breakdown cannot be prevented; it is, in fact, beneficial in cleaning and polishing the structure. What must be prevented, however, is the flow of an excessive amount of electrical energy into the fault which might lead to damage of the structure. This energy limit lies in the 10- to 100-J range.

A series switch between the output of the power supply and the accelerator has several advantages. It protects the accelerator by interrupting the fault current, which may be considerably less than the supply short circuit if the switch is fast enough or inherently current limiting. The series switch must be able to interrupt full short-circuit power for the short time required to clear the fault. The power supply remains at full output voltage, ready for instantaneous reapplication to the accelerator after the fault has cleared. A crowbar shunt switch and primary breaker may be used as backup in case the series switch fails to interrupt. We use as a fast series switch a high power tetrode vacuum tube. Existing tubes can switch up to 60 kV reliably and interrupt more than 100 A of current. The tetrode's constant current characteristic provides inherent current limiting under load fault. Operation of the tube in the negative grid region simplifies driver circuitry. The tube is biased just above saturation, with a 2- to 5-kV plate drop at operating current, allowing some supply droop regulation and supply overshoot regulation up to the tube breakdown limit. The 40-kV/30-A modulator designed and built for the ORMAK neutral beam injectors (10-cm-diam duoPIGatrons providing up to 40-kV/15-A ion beams) is shown in Fig. 40. Five such units have been built and operated successfully on test stands and on ORMAK. The modulator consists of an Eimac Y-647 tetrode switch,

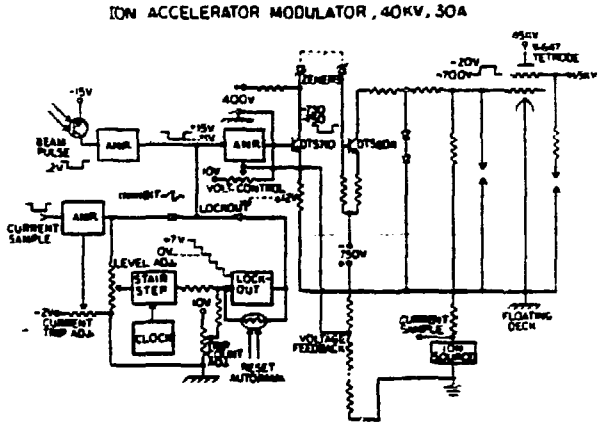

Fig. 40. Schematic of 40-kV/30-A modulator.

driven in a direct coupled circuit by a high voltage power transistor. The voltage regulation feedback loop as well as overcurrent inhibit and enable input logic are directly coupled. Fast control signals are transmitted to the floating deck via light pipes; slow control signals such as trip levels are set by potentiometers driven by insulated shafts from ground. Solid-state components on the floating deck are protected from high voltage transients through careful shielding, careful lead layout, and adequate transient suppression with varistors, diodes, and spark gaps. The modulator normally delivers a regulated high voltage to the ion accelerator. If the current sample exceeds a preset value, indicating a fault, the tube is cut off for a fixed time, interrupting the fault current. After this interrupt time the tube resumes conduction and reapplies voltage to the accelerator. This first overcurrent signal initiates a trip count clock, which permanently cuts off the tube if a preset number of overcurrent trips per unit time interval (e.g., 3 trips in 10 ms) is exceeded, indicating a possible

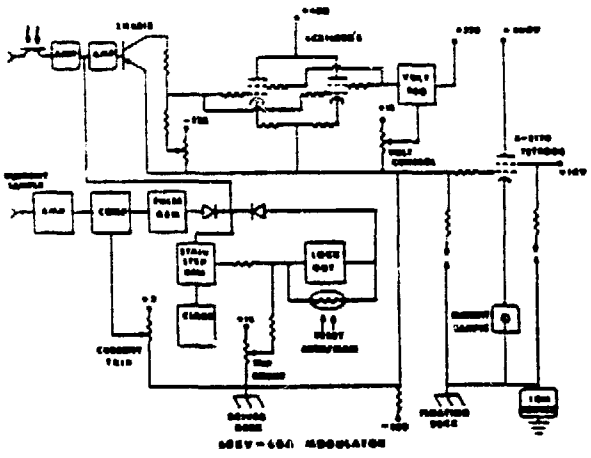

Fig. 41. 60-kV/6-A modulator.

permanent accelerator fault. This trip count clock is usually automatically reset to avoid lockout during source conditioning. Modulator rise and fall times for a normal output pulse are <50 μs.

A 60-kV, 60-A modulator was built for the development of injectors for PLT.[56] The basic circuit shown in Fig. 41 was based on the 40-kV, 15-A ORMAK modulators. The input pulse originates in a pulse generator synchronized with other commands to the neutral beam electronics system. This pulse drives a light emitting diode that is optically coupled to a phototransistor on the driver deck of the floating deck modulator. Two solid-state amplifier stages drive a high voltage switching transistor into saturation. The switching transistor provides the grid drive for two Eimac 4CX-1500-B tetrodes operating in parallel as the driver stage. A voltage regulator on the driver screen supply controls the grid drive of the final high power switch tube. The high power switch tube is an Eimac X-2170 vacuum tetrode. Spark gap protection is provided from plate to ground and from screen and control grids to cathode. In addition, the tube and ion source are protected by an electronic crowbar which fires if the switch tube fails to block an ion source breakdown. The ion source current is sampled by a current sensor isolated from the floating deck. The current sample is amplified and compared with a preset current trip level. If a fault occurs, the comparator output triggers a pulse generator that provides a pulse output of approximately 500-μs duration. This pulse interrupts the output switch tube and permits the fault to clear. The switch tube resumes conduction and high voltage is applied again to the ion accelerator. Each time the pulse generator is triggered, indicating a fault, a stairstep generator is triggered and stepped downward. A specified number of faults during a pulse can be controlled by the trip count control. When the stairstep output goes negative, the modulator is locked out for the remainder of the pulse. The function of the clock shown in Fig. 41 is to control the time interval before another pulse may be generated. Several special design requirements unique to high voltage modulator design have been considered. These include anode and filament water column resistance, filament heating rampup and rundown, energizing the screen supply only when plate voltage is present, and ensuring that adequate bias voltage is present before high voltage is applied. Noninductive resistors are used in critical locations, and bypass capacitors are utilized when required. Low level circuits are protected by varistors, capacitors, and transient absorbing Zener diodes.

A 150-kV, 50-A modulator system shown in Fig. 42 is essentially three 60-kV, 60-A modulators stacked for the series switch to the accel grid of the ion source and a shunt modulator to regulate the voltage on the gradient grid of a two-stage ion source. Modifications of the 60-kV, 60-A modulator consist of removing most of the low level protective circuits from the floating deck and locating them at ground potential. Fault current is sensed on the floating deck and optically coupled to ground. The pulse command for the three decks originates in three series-driven light emitting diodes. Delay time and rise time are carefully controlled up to the control grids of the final switch tubes. Static and transient voltage division across the separate decks is forced with resistive and capacitive dividers. A differential voltage is sampled across each switch tube and if this voltage exceeds a preset level, all tubes are forced to the blocking state. The gradient grid voltage is controlled by an Eimac Y-647 tetrode vacuum tube. As shown in Fig. 42, current flow is assumed to be away from the gradient grid of a two-stage ion source. The function of the gradient modulator is to regulate the voltage at the gradient grid. Details of the accel power supply delivering 168 kV/50 A are found in Ref. 57 (see Fig. 42).

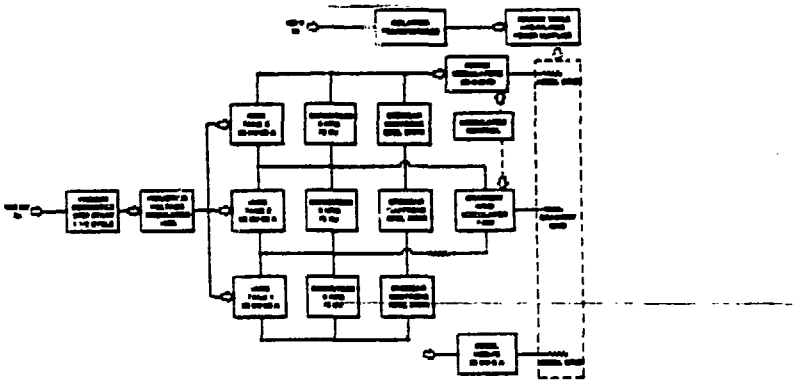

Fig. 42. 150-kV/50-A modulator.

A multichannel telemetry system has been designed and constructed to control and monitor duoPIGatron ion sources.[58] With the exception of the accelerating and decelerating power supplies, all power supplies and H_2 gas control that operate the ion source are elevated to accelerating potential. The telemetry system operates and monitors the isolated power supplies and transmits data across the high voltage gap. The transmission medium is infrared light pulsed through 10-ft-long, 1/8-in.-diam fiber optics, one end at high potential and the other end at ground potential. Conversion is accomplished by digitizing analog signals before transmitting through the optical system and demodulating at the terminating end. A maximum conversion rate of 100 kHz provides adequate resolution to operate the ion source. The output data are documented and stored in a PDP-11 computer. Although the control input is computer compatible, no attempt thus far has been made for closed loop feedback control of the ion source.

The objective of the vacuum components development program[59-62] is development and construction of integrated high speed ($\sim 10^6$–10^8 liters/s) pumping systems for near-term fusion experiments with applicability to future fusion reactor requirements. Since getters, cryosorption, and cryocondensation have many complementary characteristics, it is probable that a fusion device vacuum system would employ a combination of these techniques.

Seven cryocondensation pumps cooled by 4.2K liquid helium were fabricated for the PLT injectors by Arnold Engineering Development Center under subcontract. These were designated as types A (5 m^2), B (0.5 m^2), and C (2.5 m^2) and were installed in the source tank, drift tube, and Medium Energy Systems Test Facility (MESTF) target tank, respectively. The numbers in parentheses give the pump inlet areas. During injector system tests at ORNL, the helium consumption per pump varied from 3 to 5 liters/hr, depending on operating conditions. Continuous flow hydrogen pumping tests on a C pump indicated a maximum pumping speed of about 2×10^5 liters/s (Ref. 63) after proper ion gage sensitivity corrections were applied. No evidence of pump instability was observed during high power neutral beam pulses, and typical maximum beam line pressures remained in the range of 10^{-4} Torr. Other design and performance details are given in Ref. 63.

Construction is proceeding on a large cryosorption pump with an inlet area of 2 m^2 (Ref. 64). The pump (Fig. 43) is very similar in configuration to

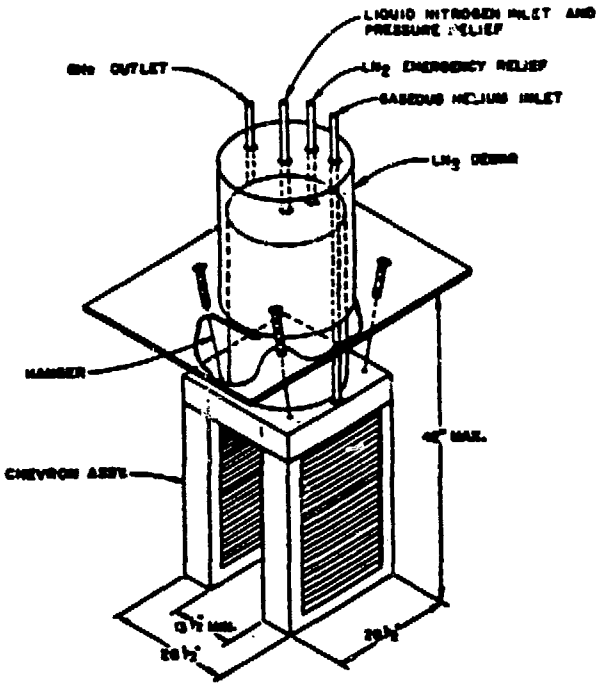

Fig. 43. Excalibur 2-m^2 cryosorption pump.

the type C cryocondensation pumps, and will be tested in the METF target chamber in direct comparison with the existing C pump. The pump is being fabricated by Excalibur Corp. of Waltham, Massachusetts. The pump panels will be maintained at temperatures between 10K and 20K by 3-atm supercritical helium gas circulated through a liquid helium bath by a room temperature compressor coupled to the cold loop through a heat exchanger. Design and most of the procurement for this loop are complete, and fabrication is proceeding.

Engineering data on molecular sieve materials for cryosorption are being obtained in collaboration with the ORNL Chemical Technology Division. Sample panels 10 cm in diameter are being tested in a variable panel/temperature cryostat (Fig. 44). The first tests were carried out on a sample of type 5-Å molecular sieve (5-Å pores) in 1.5-mm-deep grooves on a stainless steel substrate. A total of 82 5-min test runs with hydrogen gas were completed at panel temperatures ranging from 12K to 35K. No evidence of panel degradation was observed. Figure 45 gives average speeds vs pressure at various hydrogen flow rates and panel temperatures. It can be seen that the highest speeds are obtained at the lowest panel temperatures. The minimum 15K speed amounts to about 2 liters/s/cm^2 at 10^{-4} torr. This low value is due to rapid falloff of the pumping speed as material accumulates in the surface pore layers and indicates that 5-Å sieve will probably not be acceptable for fusion applications. Some preliminary tests with type Na-Y sieve (7-Å pores) on a similar stainless

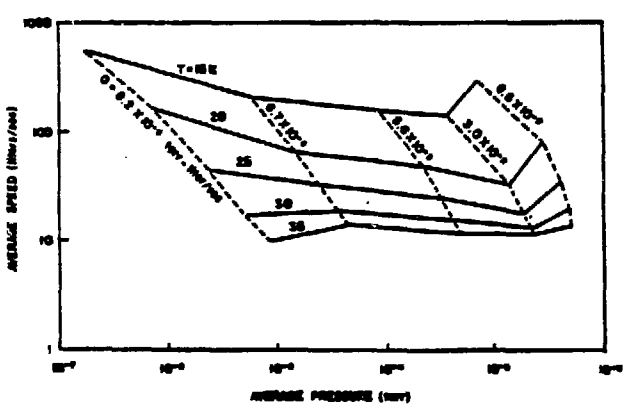

Fig. 45. Average pumping speeds for a 5-min run vs pressure for a 10-cm-diam type 5-Å molecular sieve cryosorption panel.

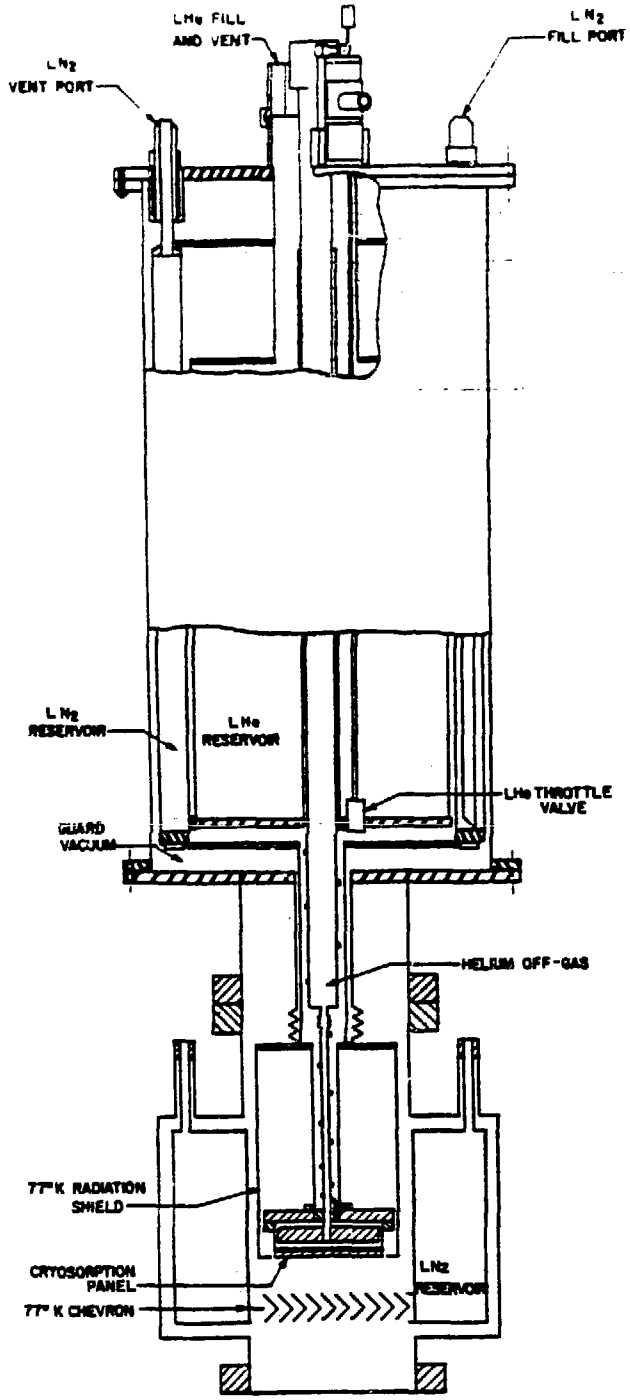

Fig. 44. Variable panel/temperature cryostat.

steel substrate indicate that larger pores give an order of magnitude better pumping speed at 15K. This sieve will be used on the 2-m^2 Excalibur pump.

The pumping systems for the divertor and main plasma chamber will have to handle gas mixtures containing as much as 15% helium produced by the fusion "burn." Pumping speed tests with a D-5% He mixture were performed on a molecular sieve 5-Å panel at 4.2K.[35] The results indicated that the sieve will not pump both gases at once — the deuterium plugs the sieve pores and the helium accumulates, leading to cryogenic runaway. When an intermediate chevron cooled with 4.2K helium gas was interposed, pumping speeds comparable to those for pure deuterium were obtained. Hence, compound pumps having separate stages for each gas component will be required for mixed gases.

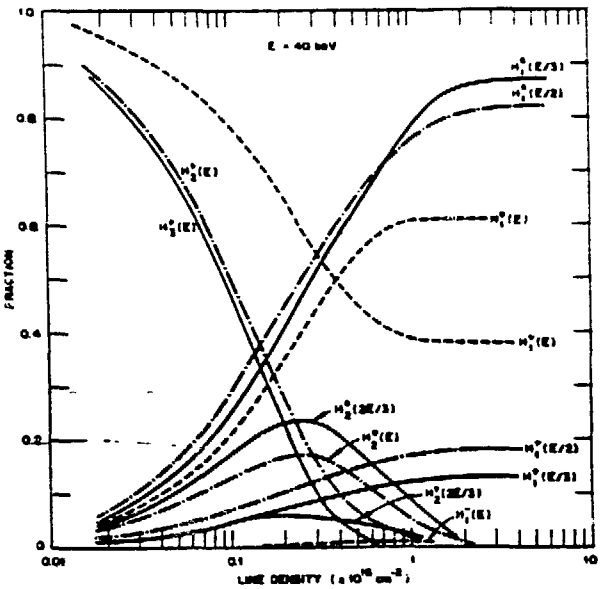

Fig. 46. Variation of fractional powers carried by particle species as a function of the downstream line density of H_2 (or D_2) for hydrogen energy of 40 keV (or 80 keV) for deuterium.

The beam power intensity distributions downstream from multibeamlet focused sources have been computed for Gaussian[43] and Lorentzian[66] beamlets. This has been done analytically using a "square peg in a round hole" approximation which rapidly converges for virtually all regions of interest. Design of beam lines is considerably facilitated by use of this analysis.

Species evolution in the neutralizer cell was examined by considering the most dominant reactions and solving the steady-state Euler level transport equations for each species.[10] Species evolution as a function of line density is shown in Fig. 46.

An analysis[67] was made of the spatial dependence of the neutral gas density due to charge exchange and ionization with the beam. The solution to the two coupled nonlinear Euler level transport equations was found by the following method. A first integral was done directly, yielding a single Bernoulli nonlinear equation. This was transformed to a linear first order equation in the inverse gas density and subsequently solved in compact analytical form. The solution (Fig. 47) was found to depend only on one parameter, μ, which is typically equal to about three. The neutral gas density due to these processes diminishes more rapidly than the fast protons even though the gas density is orders of magnitude greater than the beam density. This analysis implies that the neutral gas supply in a typical neutralizer cell is recombination dominated for an equilibrium cell. Neither pressure gradients nor recombination processes were taken into account. However, the physical insight into the neutral gas processes which this analysis affords may have a profound impact on designing beam lines — particularly pumping systems and prevention of charge exchange in the accelerating electrodes. This will have an effect on the analysis of Ref. 10 and other similar analyses[68] which assume the gas density is independent of the beam and the beam interactions with the slow positive plasma ions are negligible.

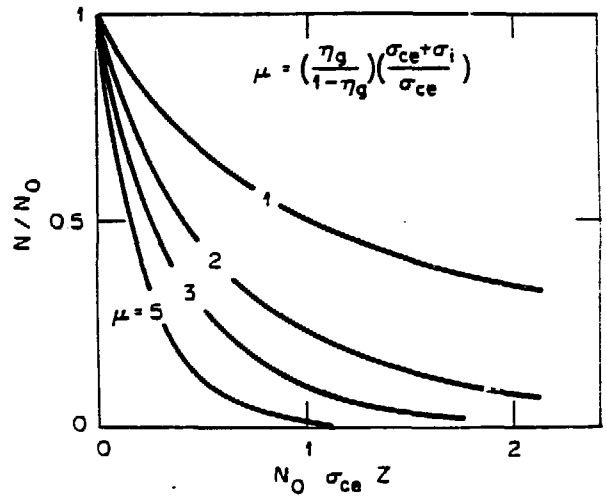

Fig. 47. Variation of gas cell neutral density as a function of distance, on the scale of the e folding equilibrium length, and a parameter shown, which is typically 2-5.

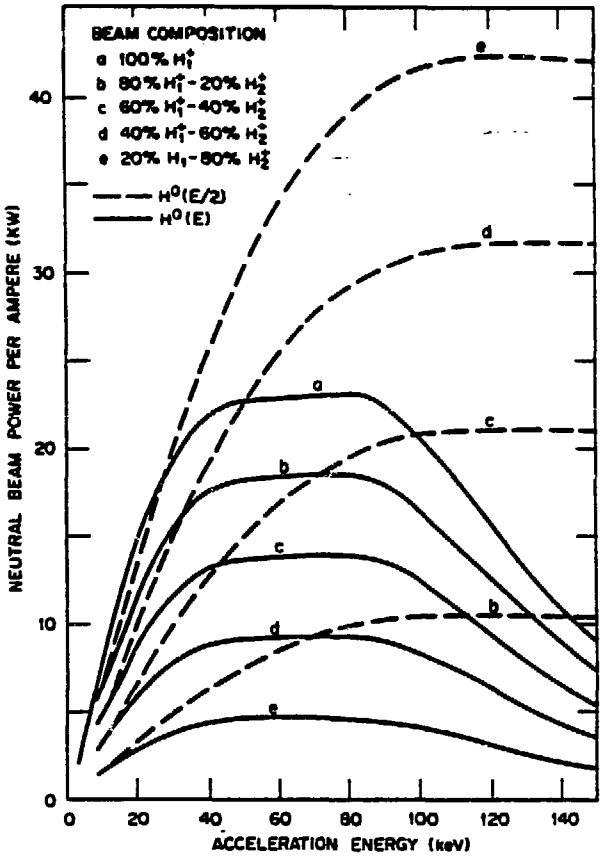

Fig. 48. Neutral beam power per ampere of the original ion beam current as a function of the beam energy for different species distributions (H_1^+ and H_2^+ only).

The nonlinearity of the inefficiency of sources producing molecular ions was delineated in Sect. 1. There the fractional energy neutrals were shown to be undesirable.[11] Here we show that they are gluttonous.[10] Below we show the potential manifestations of their unrecoverability.[12] An illustration[10] of the power distribution among the neutral components is shown in Fig. 48. It shows, for example, that at 80 keV, if half the ions are monatomic and half are diatomic, only one-third of the input power goes toward accelerating the monatomic ions. This is because the electron capture cross section is higher for the slower heavier species at 80-keV energy.

Residual space charge in the neutralizer cell was studied extending the analysis of Gabovich for high current densities, beam radii, and variations in beam composition along its path.[69] The result is that for a constant beam below the energy of the two-stream instability, the beam blowup due to residual space charge is negligible. Consideration of residual space charge blowup of a beamlet in the neutralizer leads to the conclusion that this effect may be reduced by at least a factor of four by reduction of beam perveance.[70]

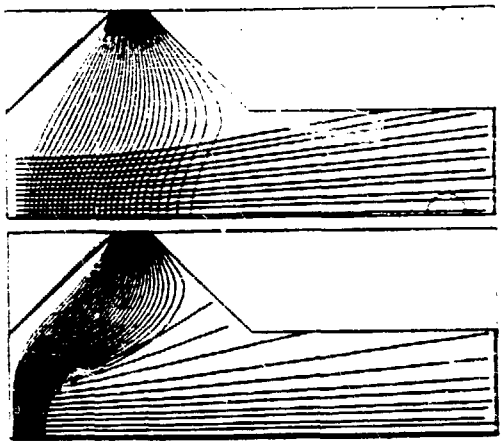

Fig. 49. Ion beam distribution and equipotential surfaces shown for a hypothetical recovery device where the ion beam density for the bottom case is 10 times that of the top case.

We are pursuing a direct recovery development based on two concepts distinguished by the electron blocking mechanism. The first is magnetic field blocking over the entire beam. The potential virtues of this scheme are indicated by the success of earlier experiments.[71] Recent theoretical calculations[72,73] solving the Poisson-Vlasov equation by the accelerating underrelaxation scheme[24] show that for sufficiently intense beams in steady state, a collector plasma forms, making the region of ion deceleration small (see Fig. 49). This small region increases the recovery efficiency since the ion beam does not get a chance to blow up and become retrograde even for very intense, high perveance beams. An illustration of potential recovery efficiency for a particular geometric configuration is shown in Fig. 50. We convinced Ralph Moir of Lawrence Livermore Laboratory of the possible success of the magnetic blocking direct recovery scheme in early 1977. He subsequently performed a test at his facility and found 50% recovery efficiency.[74]

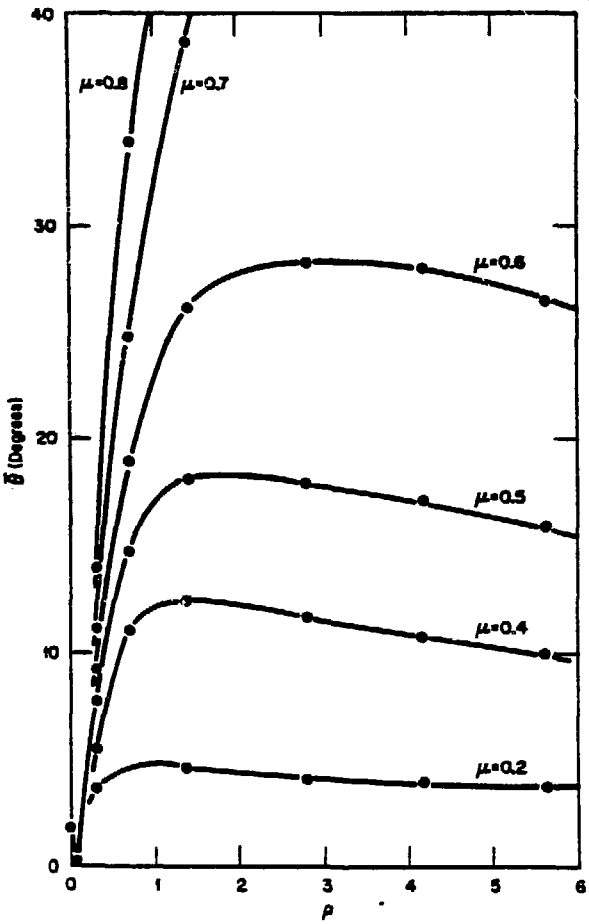

Fig. 50. Potential recovery from a geometry shown in Ref. 72 as a function of retarding voltage, on the scale of beam energy and beam density.

We showed above that the fractional energy neutrals produced from molecular ions were gluttonous[10] and undesirable.[11] Even if the geometry were such as to provide 100% recovery, a finite fraction of molecular ions would ruin this possibility because of the unrecoverable half and one-third energy neutrals which are thus produced. This is shown in Fig. 51, which illustrates recovery potential as a function of monatomic species fraction and beam energy. Also shown is the maximum efficiency without direct recovery as a function of monatomic species fraction.[12] The direct recovery experiment under way here has the ion source at ground potential and the neutralizer cell at high potential.[75]

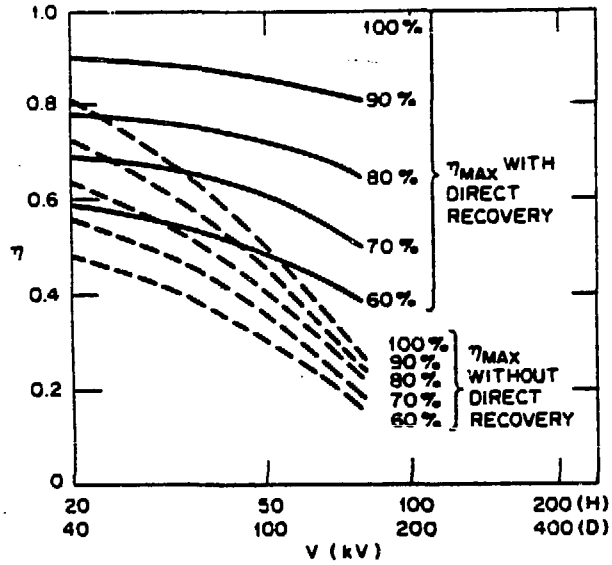

Fig. 51. Potential beam efficiency (full energy neutral production/power expended) as a function of monatomic species ratio, beam energy, and existence of direct recovery.

The drift tube has received considerable attention lately due to the possibility of a nonlinear beam attenuation resulting from gas desorption from the wall which in turn is due to deflection of the ionized beam by the stray tokamak fields (Riviere and Sheffield[76]). This analysis has been extended to include the effect of direct interception of the beam on the wall due to finite beam divergence.[77] Assuming Gaussian beamlets and using a beam intensity analysis,[43] the effect of beam divergence on reionization loss is illustrated in Fig. 52 for the system shown in Fig. 11 at various values of the specific desorption coefficient. Experiments on the drift tube pressure rise of a 30-kV, 40-A beam of pulse duration up to 500 ms[78] have been performed on the system illustrated in Fig. 11. Principal findings are: (a) the pressure buildup in the PLT drift tube is a linear function of time within a pulse and depends on beam power, (b) the pressure increase in the drift tube is substantially greater than can be accounted for by cold gas emerging from the source and is therefore attributed to gas desorption from the drift tube walls, (c) hydrogen is the principal gas desorbed from the drift tube wall, (d) pressure buildup does not change significantly as a function of cumulative pulses, (e) pressure rise time constants are characteristic of temperature variations in drift tube materials and are much longer than any other system characteristic time, and (f) pressure fall time is short compared to rise time and is similar to nonextraction pumping time constants. We deduce from this that (a) the desorption process is rapid because the pressure fall time is much shorter than the pressure rise time, and (b) the desorption coefficient, γ, is an increasing function of the temperature. The manifestation of these results is that for a 39-kV, 60-A extracted beam on our ORNL/PLT beam line, an average of >10% would be reionized and bent

back to the drift tube wall by a magnetic field, causing an additional rise in gas pressure and yet more reionization loss. A pulse length of 300 ms would increase the >10% figure to an average of >15% reionization without a magnetic field and even more with a field.

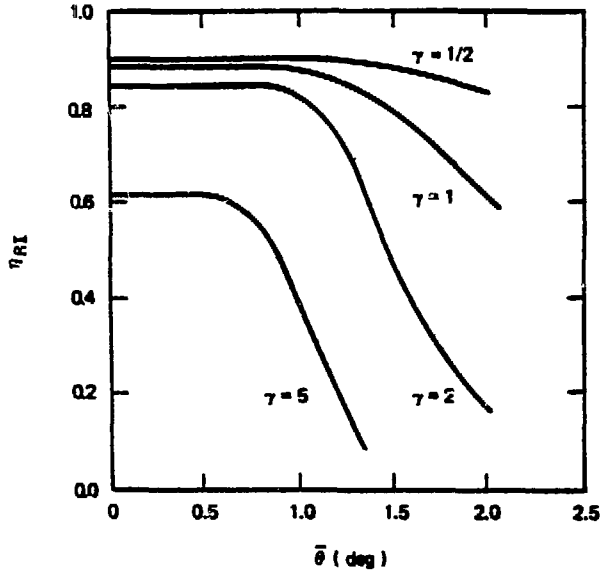

Fig. 52. Steady-state transmission efficiency through the drift tube duct as a function of the beamlet divergence and specific desorption.

Target design is important since targets may have to dissipate a power flux[63] of more than 10 kW/cm^2. Water-cooled tubes placed at an oblique angle to the beam are the basis for our principal target design (see Fig. 53). Vortex flow in a tube, produced by an internal spiral swaged ribbon, has been shown to produce a heat transfer coefficient as much as two times larger than a straight axial flow of the same fluid. It has been shown[79] that the ratio of vortex flow to axial flow burnout heat fluxes is about two and that vortex flow is most beneficial with either bulk boiling with net steam generation or local boiling with moderate subcooling. A two-dimensional steady-state heat conduction equation, accounting for the azimuthal variations in heat flux, has been carried out[80,81] to analyze the target requirements. It was found that the one-dimensional heat transfer calculations are too conservative by as much as a factor of two for the burnout heat flux.

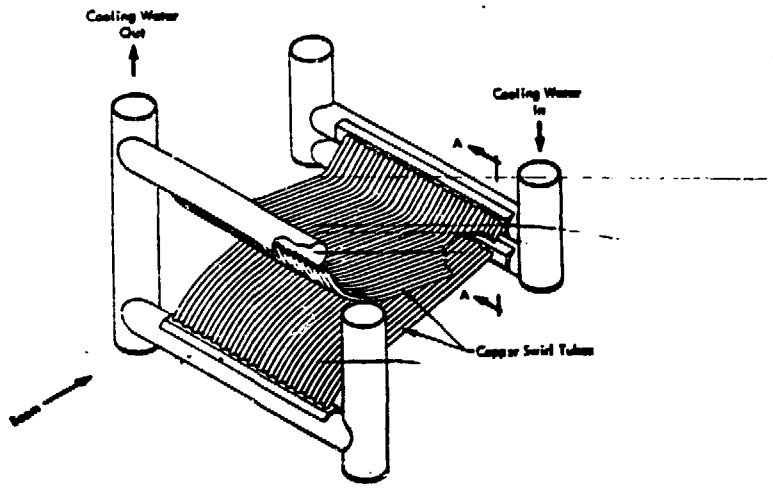

Fig. 53. Vortex flow tube target.

Swirl tube targets are currently used as a calorimeter target and a charged particle dump. The system has been run up to an "accelerator power" level of ~2 MW. From a power profile measurement at a modest beam power level (30 kV/40 A), we estimate a peak beam power intensity of 6 kW/cm^2 (both neutrals and ions in this case) with a pulse length of 100 ms at a duty factor of 1%. In this case, the water flow rate was 0.43 liters/s/tube at an inlet pressure of 250 psia and an outlet pressure of 25 psia, resulting in the axial flow velocity of 15 m/s. The nonboiling swirl flow heat transfer coefficient is estimated as h_e = 8.4 W/cm^{2}K. The copper tube dimensions are D_i = 0.633 cm and D_o = 0.902 cm. The heat transfer time constant for this case is then about 70 ms, which implies that the heat transfer is not yet fully steady state for the beam pulse length of 100 ms. The one-dimensional steady-state burnout heat flux is about 2 kW/cm^2. However, this two-dimensional computation predicts 4 kW/cm^2.

ACKNOWLEDGEMENTS

We acknowledge the help of W. R. Becraft, E. H. Bryant, M. R. Busby, D. D. Cannon, W. S. Cooper (LBL), J. S. Culver, P. W. Fisher, A. T. Forrester (UCLA), C. F. Foster, W. R. Gambill, D. M. Goebel (UCLA), L. R. Grisham (PPPL), E. F. Jaeger, R. L. Johnson, G. G. Kelley, M. H. Kunselman, K. N. Leung (MC), S. L. Milora, G. B. Morgan, E. E. Potter, C. C. Queen, J. A. Rome, G. Schilling (PPPL), D. O. Sparks, S. A. Stern, L. D. Stewart (PPPL), C. E. Thomas (MIT), P. B. Thompson, J. S. Watson, and J. C. Whitson.

REFERENCES

1. G. G. Kelley, N. H. Lazar, and O. B. Morgan, Nucl. Instrum. Methods 10, 263 (1961).
2. O. B. Morgan, G. G. Kelley, and R. C. Davis, Rev. Sci. Instrum. 4, 467 (1967).
3. G. G. Kelley, IEEE Trans. Nucl. Sci. 14, 29 (1967).
4. R. C. Davis, O. B. Morgan, L. D. Stewart, and W. L. Stirling, Rev. Sci. Instrum. 43, 278 (1972).
5. G. G. Kelley et al., Nucl. Fusion 12, 169 (1972).
6. R. C. Davis et al., Rev. Sci. Instrum. 46, 576 (1975).
7. W. L. Stirling, C. C. Tsai, and P. M. Ryan, Rev. Sci. Instrum. 48, 533 (1977).
8. C. C. Tsai, W. L. Stirling, and P. M. Ryan, Rev. Sci. Instrum. 48, 651 (1977); C. C. Tsai et al., IEEE (Knoxville 1977).
9. J. H. Whealton and C. C. Tsai, Rev. Sci. Instrum. 49, 495 (1978).
10. J. Kim and H. H. Haselton, ORNL/TM-6302 (1978).
11. J. A. Rome, Pellet Fueling Workshop (Princeton 1977).
12. J. H. Whealton and H. H. Haselton, unpublished (1977).
13. J. Kim and R. C. Davis, Appl. Phys. Lett. 30, 130 (1977).
14. W. K. Dagenhart et al., IEEE (Knoxville 1977).
15. R. Limpaukar and K. R. Mackenzie, Rev. Sci. Instrum. 44, 726 (1973).
16. W. L. Stirling, K. N. Leung, and C. C. Tsai, Bull. Am. Phys. Soc. 21, 1082 (1976).
17. P. M. Ryan, C. C. Tsai, and W. C. Stirling, Bull. Am. Phys. Soc. 22, 1083 (1977).
18. W. L. Stirling, P. M. Ryan, C. C. Tsai, and K. N. Leung, unpublished (1978).
19. W. L. Stirling et al., IEEE (Knoxville 1977).
20. D. M. Goebel, J. T. Crow, and A. T. Forrester, Rev. Sci. Instrum. 49, 469 (1978).
21. E. F. Jaeger and J. C. Whitson, ORNL/TM-4990 (1975).
22. J. S. Hornsby, CERN-63-7 (1963).
23. W. S. Cooper, K. Halbach, and S. B. Magyary, LBL-3317 (1974).
24. J. H. Whealton, E. F. Jaeger, and J. C. Whitson, J. Comput. Phys. 27, 32 (1978).
25. J. C. Whitson, J. Smith, and J. H. Whealton, J. Comput. Phys. (in press); Bull. Am. Phys. Soc. 22, 1114 (1977).
26. J. C. Whitson and J. H. Whealton, ORNL/TM-5719 (1977).
27. J. H. Whealton, E. F. Jaeger, and J. C. Whitson, Rev. Sci. Instrum. 48, 829 (1977).
28. J. H. Whealton and J. C. Whitson, unpublished; Bull. Am. Phys. Soc. 23, 151 (1978).
29. L. R. Grisham, C. C. Tsai, J. H. Whealton, and W. L. Stirling, Rev. Sci. Instrum. 48, 1637 (1977).
30. J. Kim, J. H. Whealton, and G. Schilling, J. Appl. Phys. 49, 517 (1978).
31. J. H. Whealton, L. R. Grisham, C. C. Tsai, and W. L. Stirling, J. Appl. Phys. 49, 3091 (1978).
32. A. J. T. Holmes, unpublished (1978).
33. J. H. Whealton, Rev. Sci. Instrum. 48, 1428 (1977).
34. W. L. Gardner, J. Kim, M. M. Menon, and J. H. Whealton, Rev. Sci. Instrum. (in press); Bull. Am. Phys. Soc. 22, 1082 (1977).
35. J. H. Whealton, Appl. Phys. Lett. 32, 353 (1978).
36. J. H. Whealton, unpublished (1978).
37. M. M. Menon, W. L. Gardner, and J. Kim, Bull. Am. Phys. Soc. 22, 1082 (1977); J. Kim, W. L. Gardner, and M. M. Menon, unpublished (1978).
38. L. D. Stewart, J. Kim, and S. Matsuda, Rev. Sci. Instrum. 46, 1193 (1975).
39. P. M. Ryan and J. Kim, Bull. Am. Phys. Soc. 21, 1365 (1975).
40. P. M. Ryan, R. C. Davis, W. L. Stirling, and C. C. Tsai, Bull. Am. Phys. Soc. 20, 1365 (1975).
41. C. E. Thomas, J. Kim, R. C. Davis, and P. M. Ryan, unpublished (1976).
42. M. M. Menon et al., unpublished; IEEE (Monterey 1978).
43. J. Kim and J. H. Whealton, Nucl. Instrum. Methods 141, 187 (1977).
44. J. H. Whealton, ORNL/TM-6421 (1978).
45. J. H. Whealton et al., IEEE (Monterey 1978); Appl. Phys. Lett. (in press).
46. W. L. Stirling et al., private communication (1978).
47. H. H. Haselton et al., IEEE (San Diego 1975).
48. L. Bromberg, unpublished (1976).
49. M. M. Menon, unpublished (1978).
50. J. Kim, unpublished (1977).
51. C. C. Tsai, L. R. Grisham, W. L. Stirling, and J. H. Whealton, IEEE (Troy 1977).
52. J. H. Whealton and W. S. Cooper, unpublished
53. S. Matsuda, R. C. Davis, T. C. Jernigan, and O. B. Morgan, Bull. Am. Phys. Soc. 18, 1321 (1973).
54. C. A. Foster, M. M. Menon, and J. H. Whealton, unpublished (1978).
55. N. S. Ponte and G. Schilling, IEEE (San Diego 1975).
56. G. C. Barber, N. S. Ponte, and G. Schilling, IEEE (Knoxville 1977).
57. G. C. Barber, A. Y. Broverman, et al., IEEE (Knoxville 1977).
58. R. E. Wright, IEEE (Knoxville 1977).
59. W. K. Dagenhart et al., Bull. Am. Phys. Soc. 20, 1275 (1975).
60. W. K. Dagenhart et al., IEEE (San Diego 1975).
61. D. D. Canon et al., IEEE (San Diego 1975).
62. S. W. Schwenterly et al., Bull. Am. Phys. Soc. 21, 1119 (1976).
63. S. W. Schwenterly et al., Trans. Am. Nucl. Soc. 27, 56 (1977).
64. S. W. Schwenterly, IEEE (Knoxville 1977).
65. P. W. Fisher and J. S. Watson, IEEE (Knoxville 1977).
66. J. H. Whealton, ORNL/TM-6421 (1978).
67. J. H. Whealton and W. L. Gardner, unpublished (1978).
68. K. H. Berkner, R. V. Pyle, and J. W. Stearns, Nucl. Fusion 15, 249 (1975).
69. L. Bromberg, unpublished (1976).
70. J. H. Whealton, Rev. Sci. Instrum. 49, 869 (1978).
71. G. G. Kelley and O. B. Morgan, Phys. Fluids 4, 1446 (1961).
72. J. H. Whealton, G. G. Kelley, O. B. Morgan, and G. Schilling, Nucl. Instrum. Methods (in press).
73. G. G. Kelley et al., IEEE (Troy 1977).
74. W. L. Barr et al., IEEE (Knoxville 1977).
75. W. L. Stirling, unpublished (1976).
76. A. C. Riviere and J. Sheffield, Nucl. Fusion 15, 944 (1975).
77. J. H. Whealton, H. H. Haselton, and W. L. Stirling, unpublished (1977).
78. W. K. Dagenhart et al., ORNL/TM-6374; IEEE (Monterey 1978).
79. W. R. Gambill, R. D. Bundy, and R. W. Wansbrough, ORNL-2911 (1960).
80. J. Kim, R. C. Davis, H. H. Haselton, and C. C. Queen, IEEE (San Diego 1975).
81. J. Kim, R. C. Davis, W. R. Gambill, and H. H. Haselton, IEEE (Knoxville 1977).